Superconductivity in silicon-gallium alloys

Master's thesis
University of Turku
Physics
2022
B.Sc. Ville Iso-Kouvola
Examiners:
Prof. P.Paturi
Ph.D. A.Ronzani

The originality of this thesis has been checked in accordance with the University of Turku quality assurance system using Turnitin Originality Check service.

UNIVERSITY OF TURKU
Department of Physics and Astronomy

Iso-Kouvola, Ville Superconductivity in silicon-gallium alloys

Master's thesis, 47 pp.
Physics
December 2022

Superconducting silicon-gallium (SiGa) is a promising new material with superconducting transition temperature above liquid helium temperature. SiGa can be fabricated with methods already utilized in semiconductor industry and it also enables superconductor-semiconductor hybrid structures.

In this thesis, fabrication and characteristics of superconducting SiGa alloy, fabricated via maskless focused ion beam (FIB) gallium implantation, with planar geometries including both low and high aspect ratio limits. Samples with variable implantation parameters were fabricated and characterized.

First, the FIB etch rates of silicon and silicon dioxide were determined. Additionally, implantation parameters including Ga-ion dose, beam blur and pitch were optimized during the study. Next, superconductivity was demonstrated both in broad areas and nanowires with superconducting transition temperature of approximately 6.3 K. Finally, implant modulation via resist based masking was studied but unfortunately the investigated method was not found to be viable.

Keywords: superconductivity, focused ion beam, implantation, silicon, gallium, nanowire

TURUN YLIOPISTO
Fysiikan laitos

Iso-Kouvola, Ville Suprajohtavuus pii-gallium seoksissa

Pro Gradu, 47 s.
Fysiikka
Joulukuu 2022

Suprajohtava pii-gallium (SiGa) on lupaava uusi materiaali, jonka suprajohtavuuden kriittinen lämpötila on korkeampi kuin nestemäisen heliumin. SiGa:a voidaan valmistaa menetelmin, jotka ovat jo käytössä puolijohdeteollisuudessa ja SiGa mahdollistaa myös suprajohde-puolijohde hybridirakenteet.

Tässä opinnäytetyössä tutkittiin suprajohtavan SiGa:n, joka valmistetaan maskittoman kohdistetun ionisädeimplantaation (engl. *focused ion beam*, FIB) avulla, valmistusta ja ominaisuuksia sekä suurilla että pienillä tasogeometrisilla mittasuhteilla. Näytteitä valmistettiin käyttäen useita eri implantaatioparametrejä.

Aluksi määritettin piin ja piidioksidin etsausnopeudet käytettäessä FIB:a. Lisäksi optimoitiin implantaatioparametreista ammuttujen gallium-ionien määrä (engl. *dose*), säteen sumennus (engl. *blur*) ja askelpituus (engl. *pitch*). Seuraavaksi suprajohtavuus noin 6.3 K kriittisen lämpötilan alapuolella osoitettiin sekä laajoilla alueilla että kapeissa nanolangoissa. Lopuksi implantaation modulointia resistimaskipohjaisella menetelmällä tutkittiin, mutta valitettavasti kyseinen menetelmä todettiin epäsopivaksi.

Asiasanat: suprajohtavuus, kohdistettu ionisuihku, pii, gallium, nanolanka

Contents

Introduction **1**

1 Background **2**

1.1 Superconductivity . . . 2

1.1.1 BCS theory . . . 2

1.1.2 Type-II superconductivity . . . 4

1.2 Superconductivity in covalent-bound materials . . . 4

1.3 Silicon-gallium alloys . . . 6

2 Experimental methods **9**

2.1 Focused ion beam . . . 9

2.2 Profilometry . . . 14

2.2.1 Optical profilometry . . . 14

2.2.2 Stylus profilometry . . . 16

2.3 Ellipsometry . . . 16

2.4 Cryogenic measurements . . . 18

3 Results **19**

3.1 Focused ion beam etch rate . . . 19

3.2 Effect of gallium ion dose and implantation parameters . . . 24

3.3 Optical measurements . . . 27

3.4 Nanowires and implant modulation . . . 31

4 Conclusion **44**

References **46**

Introduction

At the current rise of quantum technology new materials are being discovered and old ones further improved. As technological challenges progress, new superconductive materials with suitable properties are needed to meet the demand and enable sustainable development. For certain applications, the usefulness of superconducting technology can be increased for example by enhancing superconductive transition temperatures and by developing fabrication processes that are simple, reliable, and easy to integrate.

Silicon is the most used semiconductor material in current technology. However, superconductive silicon was first discovered only in 2006, albeit somewhat limited by a transition temperature below 1 K [1]. In contrast, superconductive silicon-gallium (SiGa) with significantly higher superconducting transition temperature (above the temperature of liquid helium) was discovered in 2010 [2]. The fabrication process of SiGa involves methods compatible with semiconductor industry enabling easy implementation. Additionally, the discovery of superconductivity in silicon substrate based materials enables development of superconductor-semiconductor hybrid devices, a key target for superconductive electronics.

In this thesis, that was produced at VTT Technical Research Centre of Finland Ltd, the fabrication of superconducting SiGa and superconducting SiGa nanowires via focused ion beam (FIB) gallium implantation is demonstrated and the feasibility of simple implant modulation method is investigated. First, essential theoretical background of superconductivity and history of covalent-bound superconducting materials are given. The theoretical background section is followed by the presentation of the experimental methods used in the thesis, including both fabrication and characterization. Finally, experimental results are presented and discussed.

1 Background

1.1 Superconductivity

Heike Kamerlingh Onnes was able to liquefy helium for the first time in 1908. After that, a couple years later in 1911, Onnes discovered that the resistivity ρ of mercury drops to zero below 4.15 K. The temperature, where resistivity of a material drops to zero, is called superconducting transition temperature T_c. He was the first to discover superconductivity. Since then, a significant part of material research in applied superconductivity has focused on search of new high temperature superconductors and understanding the mechanism of superconductivity. [3]

1.1.1 BCS theory

John Bardeen, Leon Cooper, and John Robert Schrieffer presented the microscopic theory of superconductivity, also known as the BCS theory, in 1957 [4]. BCS theory is based on an assumption that there is an attractive interaction between charge carriers due to electron-phonon coupling, which leads to the formation of Cooper pairs. Supercurrent, which is a dissipationless electric current, is carried by these Cooper pairs. Due to forming of Cooper pairs a superconducting energy gap Δ is formed in the density of the electronic states (DOS) [5].

Attraction in Cooper pair originates from phonon-mediated interaction, which has to overcome screened Coulomb repulsion to result in superconductivity. Such a net interaction potential $V(\mathbf{q}, \omega)$, can be approximated with:

$$V(\mathbf{q}, \omega) = \frac{4\pi e^2}{q^2 + k_s^2} + \frac{4\pi e^2}{q^2 + k_s^2} \frac{\omega_{\mathbf{q}}^2}{\omega^2 - \omega_{\mathbf{q}}^2}, \tag{1}$$

where e is the elementary charge, q is momentum transfer and k_s is the inverse screening length. Frequency is denoted by ω while $\omega_{\mathbf{q}}$ is phonon frequency. The first term of the approximation corresponds to the screened repulsion and the second

term is the phonon-mediated interaction. Effect of crystal structure is completely neglected. [5]

Considering that the interaction affects only electron states in a energy window $\hbar\omega_c$ around the Fermi level (here referenced as zero energy), the potential in equation (1) can be considered constant (indicated as V), and the zero-temperature superconducting gap Delta is derived from:

$$\frac{1}{N(0)V} = \int_0^{\hbar\omega_c} \frac{dE}{(\Delta^2 + E^2)^{1/2}}. \tag{2}$$

Here E is energy level and $N(0)$ is the density of states at the Fermi level for electrons of one spin orientation. When $N(0)V \ll 1$, weak-coupling approximation can be used [5]. Thus, Δ can be defined:

$$\Delta \approx 2\hbar\omega_c e^{-1/N(0)V}, \tag{3}$$

where $\hbar$ is the reduced Planck's constant and ω_c is the cutoff frequency of phonon interaction, where phonons stop pairing charge carriers. Thereby, zero-temperature superconducting gap $\Delta(0)$ and T_c are related [5]:

$$\Delta(0) = 1.764 k_B T_\mathrm{c}. \tag{4}$$

Here k_B denotes the Boltzmann constant. Furthermore, the temperature dependent superconducting energy gap $\Delta(T)$ is defined, while $T \approx T_\mathrm{c}$ [5]:

$$\Delta(T) = 1.74\Delta(0)\left(1 - \frac{T}{T_\mathrm{c}}\right)^{1/2}. \tag{5}$$

From equations Eq. (3)-(5), we can reason that increasing Δ leads to higher T_c. Furthermore, Δ can be increased by increasing parameter $N(0)V$, which $N(0)$ can be effectively increased by maximizing the carrier concentration n. Larger density of states near Fermi levels increases the number of available states for scattering and simultaneously enhances the dielectric screening [6].

1.1.2 Type-II superconductivity

As previously mentioned, superconductors have dissipationless conductivity below T_c. In addition, materials in superconducting state have magnetic properties, which highly differ from magnetic response of normal state materials. Superconductors can be classified in two types based on their magnetic properties, type-I and type-II [3].

Type-I superconductors have one superconducting phase as shown in Fig. 1 a). When the temperature of type-I superconductor drops below T_c, sufficiently low magnetic fields cannot anymore penetrate into the material. In this Meissner state, the superconductor behaves as a perfect diamagnet and has zero resistivity, unless the strength of the magnetic field H is higher than the critical magnetic field strength H_c of the material. While type-I superconductors have one phase transition, type-II superconductors have two. The first happens when H reaches the lower critical magnetic field strength value called H_{c1}, where magnetic field starts to penetrate the material by forming magnetic vortices leading to mixed state. The second takes place when H reaches the higher critical field value H_{c2}. Magnetic phase diagram of type-II superconductor is presented in Fig. 1 b), which demonstrates the characteristic second order phase transition of type-II superconductor. [3]

1.2 Superconductivity in covalent-bound materials

Most superconductive elements have well defined crystal structure with high symmetry. For example, face centered cubic (fcc), hexagonal close-packed (hcp) and body-centered cubic (bcc) lattices are very common for superconducting elements [3]. Group-IV elemental semiconductors have aforementioned crystal lattices and superconductivity in them was first predicted already in 1960s by Marvin L. Cohen [6]. His theoretical approach based on BCS theory indicated that there are potential superconductors in the group-IV semiconductors. He predicted that by increasing

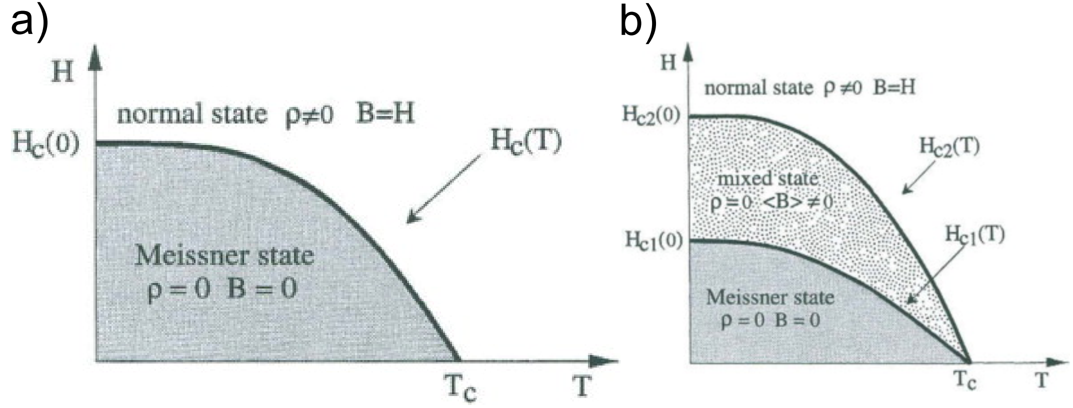

Figure 1. a) Schematic phase diagram illustrating the temperature dependence of critical magnetic field strength of type-I superconductor. b) Schematic phase diagram illustrating temperature dependence of critical magnetic field strength of type-II superconductor. Here magnetic field strength is H, magnetic flux density is B and electrical resistivity is ρ. [7]

the small density of free electric charge carriers in them at low temperatures would lead to appreciable superconducting transition temperature, since according to BCS theory large density of states at the Fermi level and strong charge carrier-phonon coupling are essential for Cooper pair formation at higher temperatures.

40 years later, this prediction was confirmed experimentally by Ekimov et al. [8] discovering type-II superconductivity in heavily boron-doped diamond. They reported superconducting transition temperature of 4 K with maximum critical magnetic field and critical current density of $B_{\mathrm{c}} = 3.5$ T and $J_{\mathrm{c}} = 0.145$ kA/cm^2, respectively. Critical magnetic field B_{c} for a given temperature is a magnetic field above which the material loses its superconductive properties and similarly critical current density J_{c} for a given temperature is maximum current density through material above which power dissipation starts to occur. Following these results, type-II superconductivity has been discovered in other doped group-IV semiconductors, including germanium and silicon. Critical temperature T_{c} of 3.5 K has been reached for copper-doped germanium and T_{c} of 0.35 K for boron-doped silicon [1, 9]. This kind of hole-doping creates p-type semiconductors where hole-type charge carrier density

is increased compared to intrinsic semiconductor values. High dopant concentration is common between all of these covalent group-IV superconductors.

Moreover, high dopant concentration is needed to increase the number of free charge carriers, holes in this instance, so that metal-insulator transition (MIT) does not occur. MIT occurs when, at low temperature, the density of charge carriers falls below a critical charge carrier concentration value n_{MIT}. For superconductivity, the carrier density must be high enough to create a conducting state at low temperatures. Superconducting state may be reached with high dopant concentrations, since increasing the density of charge carrier states increases strength of the hole-phonon coupling. It has been also shown that increasing disorder in the material leads to stronger charge carrier-phonon coupling and therefore enhances the critical temperature in superconductors obeying BCS theory [10]. However, excessive amounts of disorder will result in charge carrier trapping and eventually MIT. For disordered superconductors, reaching optimally high critical temperatures requires careful control of the amount of both dopants and disorder.

1.3 Silicon-gallium alloys

Silicon is a group-IV semiconductor which is insulating at low temperatures. Doping is needed already to avoid conventional charge freeze-out. Furthermore, to reach superconductivity even higher concentration of dopants is needed. This can be problematic since the equilibrium solubility limit of dopants is often low. [11]

Type-II superconductivity in gallium implanted silicon was reported in 2010 by R. Skrotzki et al. [2]. Superconductivity is reached by implanting $4 \cdot 10^{16}$ cm^{-2} gallium ion fluence with 80 keV energy into silicon substrate with silicon-dioxide layer on top. After implantation rapid thermal annealing (RTA) is performed to induce gallium diffusion which gives rise to precipitation of gallium into small clusters due to its low equilibrium solubility limit in silicon corresponding to Ga concentra-

tion of approximately only 0.1 % [12]. The gallium concentration before the RTA was approximately 10 % and after the RTA gallium diffusion and precipitation approximately doubled the gallium concentration near the surface at the silicon-oxide interface close to 20 % [13, 14]. This method led to T_c of 7 K, critical magnetic field B_c over 9 T and critical current density J_c over 2 kA/cm^2. Compared to other similar covalent-bound superconductors described in previous Sec. 1.2, SiGa has desirable and sizeable T_c, B_c and J_c.

As mentioned above, during the ion implantation the crystalline structure of silicon is damaged and it becomes amorphous inside the penetration depth of gallium ions, which depends on the used implantation energy as Borgardt et al. [15] have shown. They implanted high dose ($5 \cdot 10^{17}$ cm^{-2} corresponding to 800 pC/µm^2) of Ga-ions to silicon and confirmed that the amorphous layer is up to 60 nm thick with 30 kV acceleration voltage, while the maximum constant gallium concentration reached saturates at approximately 50 % in the first 25 nm after which the gallium concentration rapidly decreases as shown in Fig. 2. The origin of this saturation effect is explained later in the Sec. 2.1.

The fabrication method quoted in reference [2] requires thermal annealing for superconductivity. Moreover, some kind of lithography process is needed to form superconducting electrical components and circuits. Matsumoto et al. [16] used maskless FIB gallium implantation method as a direct patterning technique of superconducting SiGa without RTA by implanting very high $5.7 \cdot 10^{18}$ cm^{-2} fluence of gallium into silicon with 30 kV acceleration voltage and reached T_c of approximately 7 K. This method removes two time-consuming steps from the fabrication process. Notably, since thermal annealing is not needed, silicon is still in amorphous form when the fabrication process is finished.

Critical temperature T_c values reached with SiGa are close to approximately 6 K T_c of elemental β-Ga that is supercooled form of gallium with monoclinic unit cell

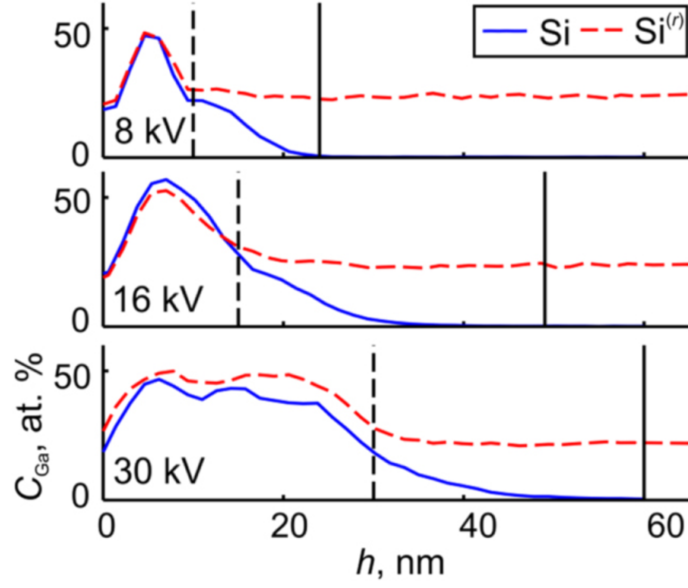

Figure 2. Mean gallium concentration C_{Ga} as a function of implantation depth h in crystalline silicon (Si) and redeposited material ($\mathrm{Si}^{(\mathrm{r})}$) with three different acceleration voltages (8 kV, 16 kV and 30 kV). The Ga implantation depths and boundaries of amorphized regions in crystalline silicon are indicated with the dashed and solid vertical lines, respectively. [15]

structure [17]. Therefore, Matsumoto et al. [16] compared the critical fields of both materials and noted that over 9 T B_{c} of SiGa is much higher than 57 mT of β-Ga according to the literature [2, 17]. They also considered the effect of the substrate and to confirm that superconductivity was also dependent on the substrate, various other substrates, including for example diamond that had already earlier shown superconductivity when doped, were explored by implanting similar amount of Ga-ions as before. Regardless of the implantation, none of the studied substrates showed superconductivity, which suggests that superconductivity in SiGa does not originate from gallium but rather from SiGa alloy.

2 Experimental methods

2.1 Focused ion beam

Focused ion beam is a nanofabrication and analysis tool that is highly used in semiconductor industry and materials science. FIB tools are capable of implantation, etching and deposition without need for any additional masking or lithography while simultaneously allowing for high-resolution imaging. The operating principle of the FIB consists in accelerating charged ions in a fine beam towards the sample, where energetic ions interact with the sample material. Depending on the details of the interaction between high-energy ions and the sample, the accelerated charges can generate characterization signals including secondary electrons and x-rays used for electron microscopy and energy dispersive spectroscopy (EDS), or significantly alter the sample itself: such as the case for etching and implantation application. [18, 19]

Some level of damage, that can be controlled by selecting viable beam settings, is always inflicted to the target sample through above mentioned interactions. Sputtering, that leads to etching or so called surface milling, results from energy transfer between incident beam ions and target surface atoms. The kinetic energy of ions is transferred to sample atoms through elastic collisions in cascades which form in the sample. A surface or near surface atom can be ejected after receiving kinetic energy greater than surface binding energy of the surface, leading to sputtering yield, defined as the number of ejected particles per incident beam ion. Sputtering depends on the dose denoting amount of ions absorbed, the target material and the incident angle of the ion beam, set perpendicular related to sample in this study. The strength of bonds in the material is the main material characteristic affecting in the sputtering rate, since tightly bound atoms are more difficult to eject. [18]

Another effect linked to sputtering is redeposition of sputtered material back to the sample surface, including both implanted ions and sample surface atoms,

resulting in altered surface composition and topography. Redeposition depends on the kinetic energy of the sputtered particles, features of the sample such as surface topography and the geometry being etched. [18]

Increasing the ion energy leads to increase in the ion stopping range in the sample material, which leads to decrease in sputtering and more efficient and deeper implantation. Essentially, the maximum momentum transfer that is required to dislocate the target atoms is obtained when the incident ions have low energy that is, when they are almost stopped. At high acceleration, this happens deep into target, so that the ejected atoms cannot be expelled in to the vacuum. Through these interactions ions will eventually come to rest and start to accumulate in the target material. In comparison, at low acceleration, the conditions for dislocating atoms are already realized at the surface, and it is relatively probable for an incoming beam ion to eject target material from its surface. At high doses and typical acceleration voltages, FIB implantation has limited implantation concentration due to continuous sputtering which leads to steady state implantation, which is an equilibrium condition, where constant implant concentration is created between target surface and maximum implantation depth. This concentration is inversely proportional to the etching rate. Therefore, materials with lower etching rate will have higher maximum implant concentration limit. [18, 20]

A secondary effect of ion implantation can be amorphization of the target surface. Collision cascades formed by incident ions induce disorder in material structure and an amorphous phase can be developed in the surface layers of formerly crystalline material. Amorphization during implantation is dependent on the defect density that must reach a critical threshold value specific for the material. Defect density further depends on the recombination rate of the defects, which is dependent on temperature. Therefore, amorphous phases do not always occur. [20]

In addition to etching and implantation, deposition of metals with FIB, known

as ion beam induced deposition (IBID), can be used to deposit metal films on the surface of the target sample. Deposited metals, usually platinum (Pt) or tungsten (W), are stored as organometallic gas compounds. The IBID process illustrated in Fig. 3 begins with spraying and adsorption of precursor organometallic gas to the surface of the sample via gas injection system (GIS) needles inserted near the surface. The adsorbed layer is then bombarded with ions resulting in desorption of volatile components. Thus, non-volatile metals are left to the surface while the organic components vaporize. However, the resulting metal layer includes residues of organic compounds and incident ions. Energetic ions will also damage the surface even though it is covered by adsorbed layer. Damage can be reduced by taking advantage of a less destructive low energy electron beam induced deposition (EBID) that can be done with a dual-beam FIB tool. EBID process is analogous to the IBID, only electrons are used instead of ions, which leads to less damage and contamination, but also in slower deposition rate. [18]

A typical dual-beam FIB consists of vacuum chamber with ion and electron columns inserted inside. Additionally, inside the chamber is a movable sample stage, detectors and GIS for deposition and enhanced etching. A liquid metal ion source (LMIS) for the ion beam is located in the ion column while vacuum pumps, that are needed to reach vacuum in the chamber and beam columns, are outside of the chamber with a computer used to operate the FIB system. [18]

One of the columns is typically mounted vertically for example the electron column in Helios NanoLab DualBeam 600 FIB/SEM, the FIB model from FEI that we used in the present thesis that is later in the text referred as Helios 600. Since there is no room for both beams to be vertical and point at the same spot on the sample, the ion column must be tilted to an angle, which is 52° for Helios 600. This way it is possible to find a coincident point where electron and ion beams intersect, allowing concurrent ion milling and scanning electron microscopy (SEM) imaging of

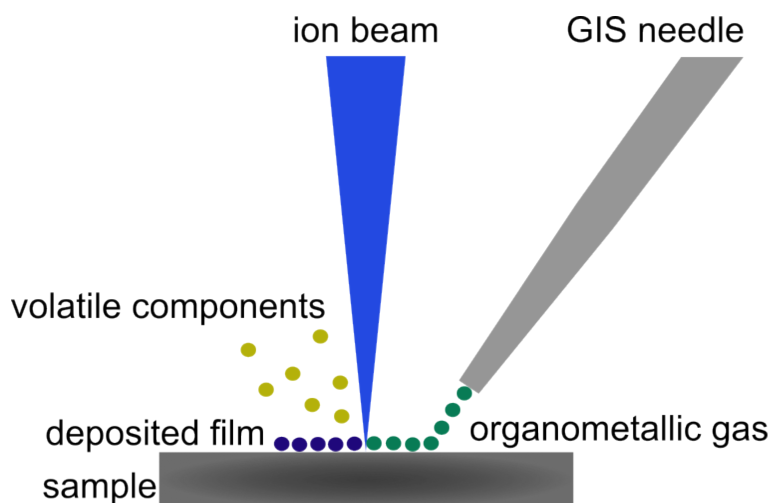

Figure 3. Principle of IBID process illustrated.

the desired area. Having both columns in one tool enables multiple use cases which include for example cross-sectioning and transmission electron microscope (TEM) lamella sample preparation [18]. A schematic diagram of dual-beam FIB chamber with instruments is presented in Fig. 4.

The structure of the ion column is similar to electron column by including electrostatic lenses and apertures as main components, however the ion beam is formed by LMIS, as illustrated in Fig. 5 a). The LMIS has a reservoir of source metal that is heated to form a liquid phase. The heated liquid metal then diffuses along a tungsten needle inserted in the reservoir. Further, a strong electric field, order of 10^8 V/cm, is applied to the tip of the needle and a stable Taylor cone shaped point source is formed through a combined result of electrostatic and surface tension forces. Ions are then extracted from the tip of the cone by an extraction voltage defining the emission current, which is typically 1-3 μA. [18]

High voltage, which typically range from 5 to 50 keV, is used to accelerate ions extracted from the LMIS in the column. Typically, ion columns are equipped with two electrostatic lenses of which the first is called condenser lens and the second objective lens, as shown in Fig. 5 b). The condenser lens forms parallel ion beam and

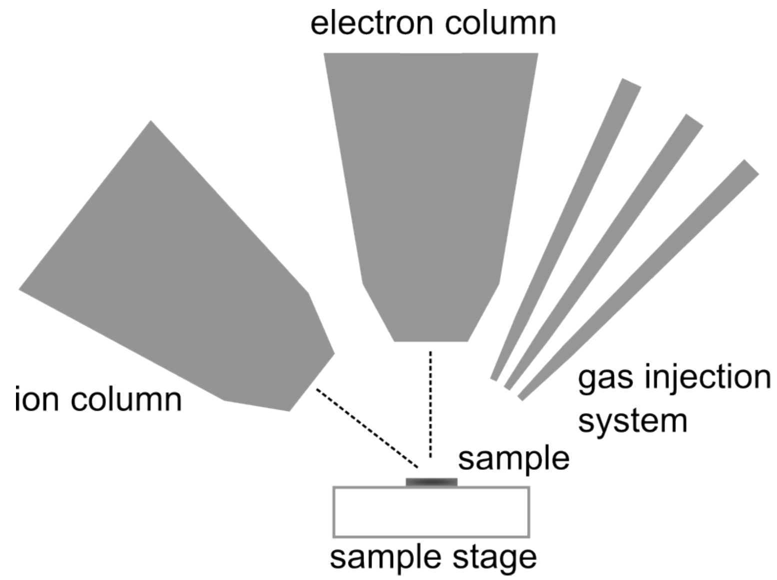

Figure 4. Schematic of dual-beam FIB chamber with beam columns, sample stage and retractable GIS needles. In addition, imaging detectors, which are not presented in the schematic, are located in the vacuum chamber.

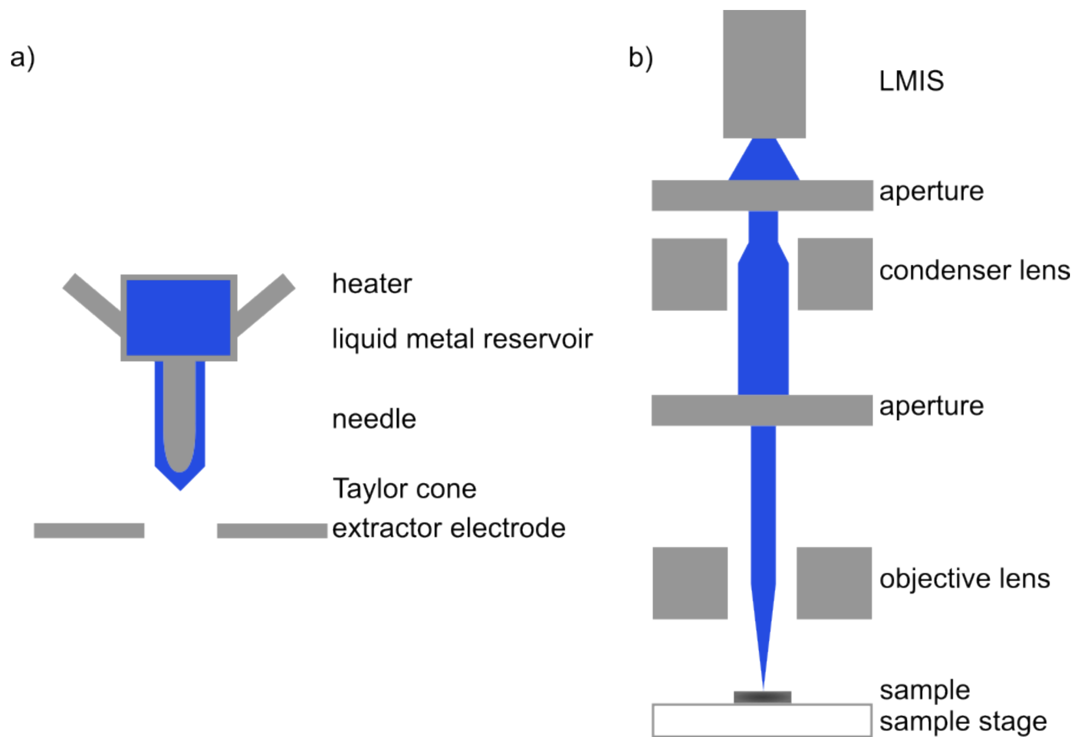

Figure 5. Simplified schematic diagrams of a) LMIS and b) ion beam column.

the objective lens focuses the beam to the sample surface while multiple apertures are used to limit beam size and adjust ion current by blocking incoming ions. [18]

The Helios 600 tool we used in this study has the above described dual-beam configuration including Ga-ion beam and electron beam. We used the ion beam for Ga implantation, etching and deposition of Pt while the electron beam was used for SEM imaging to characterize the results of the fabrication process since imaging with electrons is less destructive than with the heavier Ga-ions. FIB implantation parameters pitch and blur, which determine step size on the implantation raster and beam spread based on defocus of the ion beam, were altered. Pitch and blur have an effect on the final surface uniformity by smoothing out edges and beam raster pattern.

2.2 Profilometry

Measuring surface profile is important in many occasions and in this study surface etching rates were measured to optimize the fabrication process of SiGa. Due to material properties, two different profilometry methods were utilized.

2.2.1 Optical profilometry

Initially, we used a Bruker Contour GT-X optical profiler which is based on interferometry, since optical measurements allow fast nondestructive noncontact surface topography mapping. The tool utilizes the Mirau interferometer configuration shown in Fig. 6, which allows measurement through detecting changes in the optical phase. In the tool a light is collimated by the first lens and then split into two beams with a semitransparent beam splitter mirror. One of the beams travels through the beam splitter mirror and reflects back from the sample surface, and the other reflects from the beam splitter to a reference mirror from which the light is redirected back to the beam splitter. Beams from the sample and the reference mirror are then interfering

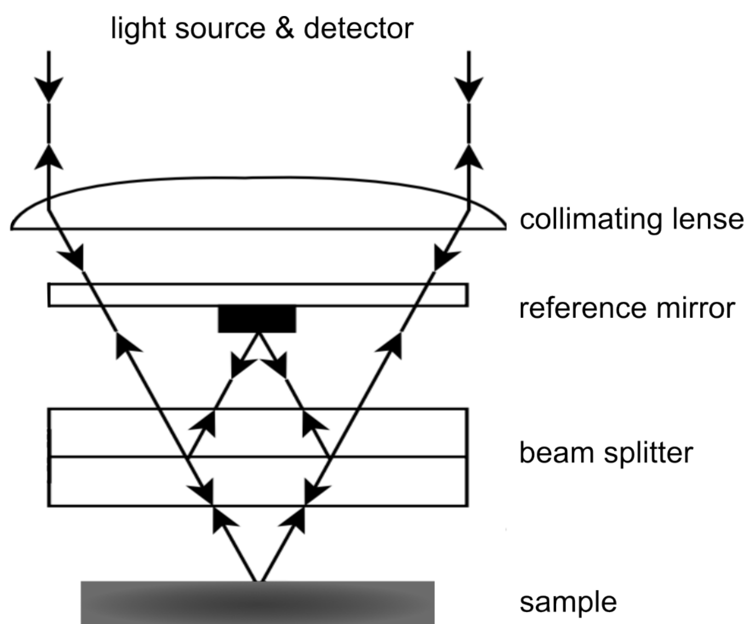

Figure 6. Mirau interferometer scheme. Modified from image in [23].

at the beam splitter, hereafter detected by a charge-coupled device (CCD) used as detector. [21, 22]

This tool supports both vertical scanning interferometry (VSI) and phase scanning interferometry, of which the first mentioned was optimal for our case, because the detected interference pattern in PSI mode becomes hard to analyze with large surface step sizes that are expected on the etched patterns. VSI on the other hand has larger vertical scanning range, which allows measurement of larger height differences on the sample surface. In VSI mode the sample is scanned with a broadband white light while the reference mirror is moved vertically to find the interference maximum of each point on the sample. Light has travelled the same distance through the reference mirror and the sample surface at the interference maximum, therefore the sample height can be determined by knowing the distance between the beam splitter and the reference mirror. [21]

However, these results originate from the interference of light, and optical characteristics of the studied material may have an effect. Multiple reflections may happen

in the material if the studied material is transparent to light, such as SiO_2. Those reflections from different layers of the sample make the data analysis much more complicated. [23]

2.2.2 Stylus profilometry

Problems related with optical characteristics of the studied material can be overcome with mechanical stylus profilometry, where a physical diamond tip is dragged along the sample surface, the downside being the potential contact contamination of the sample. While scanning, the tip moves vertically according to the surface profile and the profile can be measured with a single scan along the chosen path. Vertical movements of the tip are transformed to electrical signal usually with a linear variable differential transformer (LVDT) that converts linear movement to electrical signal proportional to vertical displacement. We used Bruker DektakXT stylus profiler with the above described properties in this study. [21]

2.3 Ellipsometry

To further characterize electrical, optical and structural properties of the studied material we used an optical measurement method called spectroscopic ellipsometry. Ellipsometer consisting of monochromatic light source, polarizer, analyzer and detector illustrated in Fig. 7 is based on measuring the change in polarization of light transmitting through or reflecting from a sample. Light from the source is first linearly polarized and then elliptically polarized in the sample. The change in polarization is then detected with the analyzer and the detector. The SE-2000 tool we used supports variable incidence angle and multiple wavelengths ranging from ultraviolet (UV) to near-infrared (NIR). [23, 24]

The measurable quantity ρ_R is equal to the ratio of the parallel component of complex reflection coefficient R_p and the vertical component of complex reflection

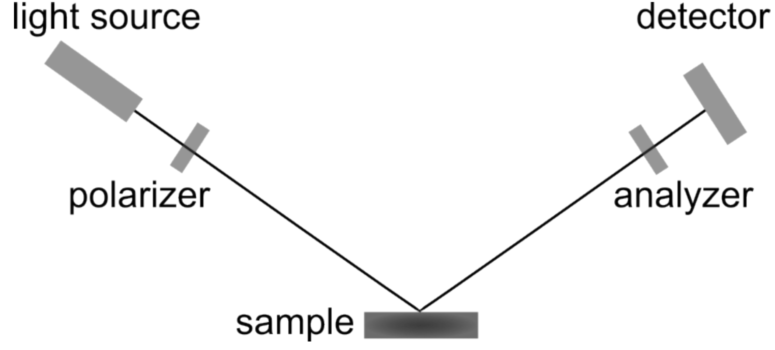

Figure 7. Ellipsometry scheme, where: light is linearly polarized in a polarizer, light reflects from the sample and is elliptically polarized and finally change in the polarization is observed with a analyzer and detector.

coefficient R_s:

$$\rho_R = \frac{R_p}{R_s} = \tan\Psi e^{j\Delta}, \tag{6}$$

where Ψ and Δ are ellipsometric angles describing change in amplitude and phase, and j is the imaginary unit. Knowing these quantities makes it possible to determine the dielectric function and layer thickness in a stack of the studied material. [23, 24]

To find the dielectric function a suitable model must be fitted to the experimental data. In the case of SiGa, we limit to a Drude free-electron model, adequate for simple conductors in the infrared limit. For lossy medium the Drude free-electron model complex dielectric function, that consists of real and imaginary parts, is presented as a function of photon frequency ω:

$$\varepsilon_c(\omega) = 1 - \frac{\omega_p^2}{\omega^2 + j\omega\gamma}, \tag{7}$$

where ε_c is the complex permittivity, ω_p is the plasma frequency and γ is the collision frequency of electrons [25]. Further, the energy E can be presented as a function of frequency

$$E = \frac{h\omega}{2\pi} \tag{8}$$

as the Planck relation suggests [26], where the Planck constant is denoted by h.

Therefore, the dielectric function Eq. (7) can be presented as a function of energy

$$\varepsilon_c(E) = 1 - \frac{E_p^2}{E(E + jE_\gamma)}, \tag{9}$$

where photon energies corresponding to the plasma frequency and electron collision frequency are denoted by E_p and E_γ. Fitting this model to experimental data leads to determination of complex dielectric function parameters E_p and E_γ.

Based on the above derived parameters, the electrical resistivity ρ and charge carrier concentration n of the material can be accessed from the Drude model:

$$\rho = \frac{E_\gamma \hbar}{\varepsilon_0 E_p^2} \tag{10}$$

and

$$n = \frac{m^* \varepsilon_0 E_p^2}{\hbar^2 e^2}. \tag{11}$$

Here ε_0 and e are denoting the vacuum permittivity and the elementary charge, whereas m^* is the effective mass of the charge carrier. [27]

In addition to all the above mentioned, complex refractive index and thickness of the material can be solved via data analysis of ellipsometric measurements. Being an optical technique, ellipsometry is non-destructive method but it has some limitations. The studied material must be transparent on some level and have fairly flat surface. Also, an appropriate physical model for the material must be available to be fitted to the experimental data. [24]

2.4 Cryogenic measurements

Superconductivity was studied by decreasing the temperature of the sample below its superconducting transition temperature, simultaneously measuring changes in the resistance of the sample. We used Oxford Instruments Heliox AC-V closed cycle He^3 adsorption cryostat, capable to reach temperatures near 300 mK, to cool down the samples and adopted a typical four-point measurement geometry.

Absolute resistance can be determined easily with four-point measurements while with two-point measurement geometry shown in Fig. 8 a) obtained total resistance R_T is combination of resistances according to Ohm's law:

$$R = \frac{V}{I}, \tag{12}$$

where R is resistance, V is voltage and I is current. Thus,

$$R_\mathrm{T} = \frac{V}{I} = 2R_\mathrm{W} + 2R_\mathrm{C} + R_\mathrm{DUT}, \tag{13}$$

where R_W is resistance of the measuring wire, R_C is the contact resistance and R_DUT is the resistance of the device under test (DUT). Since, the resistance of measuring wires and the contact resistance are not know, it is not possible to determine R_DUT accurately with more simple two-point measurements. Hence, we used the four-point measurement illustrated in Fig. 8 b), where voltage is measured with two separate contacts. Due to the high impedance of the voltage meter, current flow through it is very low. Therefore, the voltage drop in the contacts and wires are negligible and the resistance of the sample is directly accessible from the voltage measurements. [23]

3 Results

3.1 Focused ion beam etch rate

The study was started by investigating out the Ga-ion beam etch rate of Si and SiO_2. First, we implanted Ga with FIB on 675 µm thick crystalline high-resistivity silicon chips and on a 287 nm thick SiO_2 layer that was grown by thermal oxidation process on top of crystalline high-resistivity silicon. Etch rates of Si and SiO_2 were needed for determination of the dose needed to etch SiO_2 layer fully and to determine effective implant dose reaching silicon through oxide layer shown in Fig. 9. Ga implantation and simultaneous etching was performed on 10 µm by 10 µm squares with 30 kV

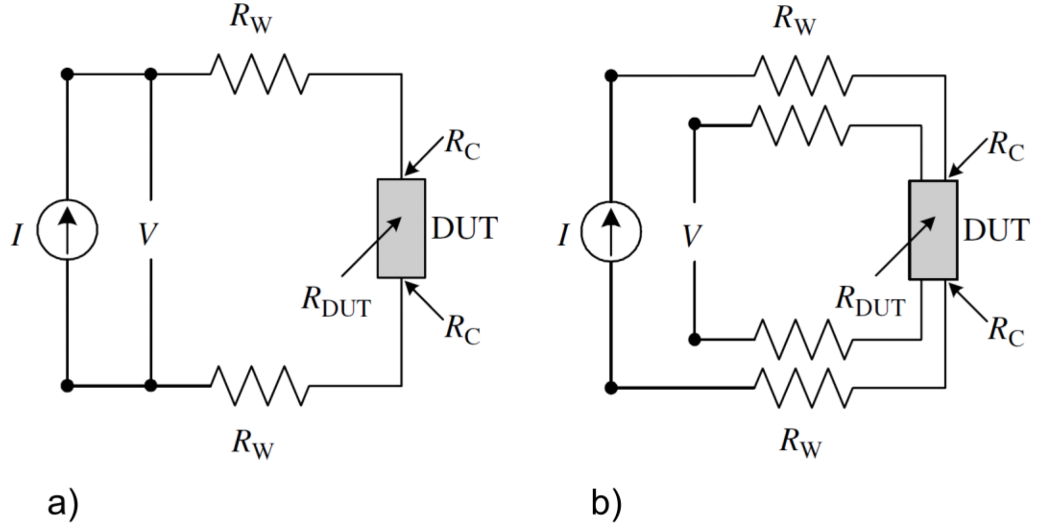

Figure 8. Two-point a) and four-point b) measurement arrangement for device under test (DUT) with current source I and voltmeter V. Here resistance of the DUT is R_{DUT}, wire resistance is R_{W} and contact resistance is R_{C}. [23]

acceleration voltage and 0.46 nA current. FIB implantation parameters pitch and blur were set to approximately 100 nm and 200 nm, respectively. Implantation was repeated ten times on both Si and SiO_2 surfaces with ten different doses ranging from 100 pC/µm^2 to 1000 pC/µm^2 in 100 pC/µm^2 increments.

After the implantation the etched depth was measured, first with the optical method described in Sect. 2.3. For characterization of bare silicon substrates, the results were clear as can be seen from Fig. 10, where etch with dose 200 pC/µm^2 is presented. However, we were not able to get clear results for SiO_2 as can be seen from Fig. 11 presenting gathered optical results for same dose as above used for Si. These misleading results are probably related to additional reflections in SiO_2 layer due to its transparency, and therefore, additional mechanical stylus profilometry measurements were performed for the samples. All results from both optical and mechanical stylus profilometry showing etched depths are presented in the same Table I below.

Then experimental data in Table I was plotted and it is presented in Fig. 12,

Figure 9. Schematic structure of the sample stack with SiO_2 layer on top of silicon substrate.

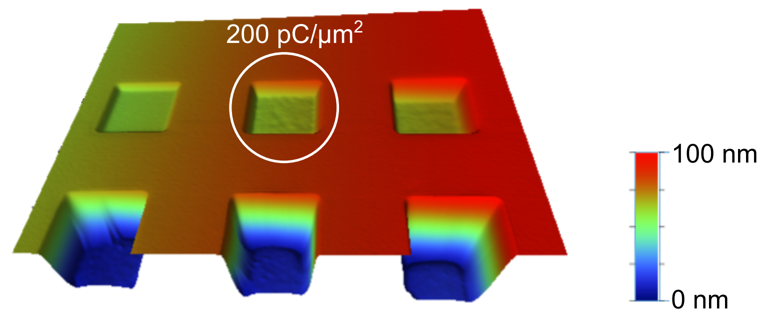

Figure 10. 3D image of optically performed etch rate measurements of silicon. Result for the implantation done with dose 200 pC/µm^2 is highlighted with a white circle.

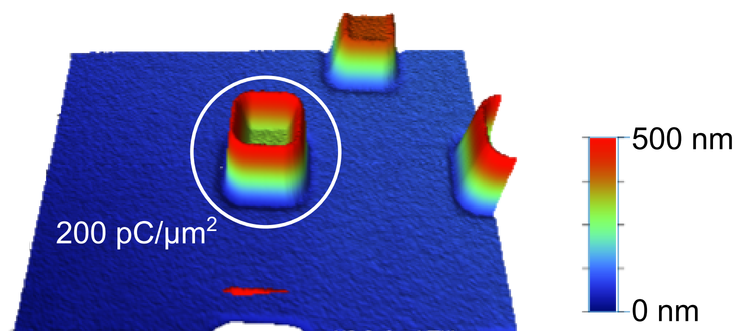

Figure 11. Optical measurement results for etch rate test on transparent oxide shown as 3D image. Result for the implantation done with dose 200 pC/µm^2 is highlighted with a white circle. Due to optical properties of SiO_2, optical measurements did not produce reliable data.

Table I. Measured etch depths z and corresponding doses for Si and SiO_2.

Dose [pC/µm^2]	z_{Si}(optical) [nm]	z_{Si}(stylus) [nm]	z_{SiO_2}(stylus) [nm]
100	25	22	
200	50	42	27
300	79	71	49
400	111	97	76
500	144	125	104
600	173	152	128
700	208	185	147
800	238	218	182
900	267	250	198
1000	298	276	208

where the etched depth z is presented as a function of the dose. Measurement results for Si were well in line with both methods and reasonable values were also obtained for SiO_2 with optical profilometry. Clearly, the etching process is linearly proportional to the dose and therefore a linear fit was done for each measurement set as shown in Fig. 12. However, the measurements done for SiO_2 etched with the two highest doses deviated more than other measurement points and it seemed like the measurement results started to saturate. Therefore, these two measurement points were neglected in the linear fit. Most likely the observed saturation was related to the performed SiO_2 etch, since similar saturation was not observed in Si etch depth measurements measured with the same tool. We obtained average volumetric etch rates of approximately 0.3 µm^3/nC $\pm$ 0.01 µm^3/nC and 0.25 µm^3/nC $\pm$ 0.02 µm^3/nC for Si and SiO_2 respectively from the slopes of the linear fits. Uncertainties of these values were reported with 95 % confidence level and determined etch rates are similar to values reported in literature [15, 28]. However, especially with SiO_2 deviations in etch rate must be expected as can be seen from the plot. Plotted linear fits do not

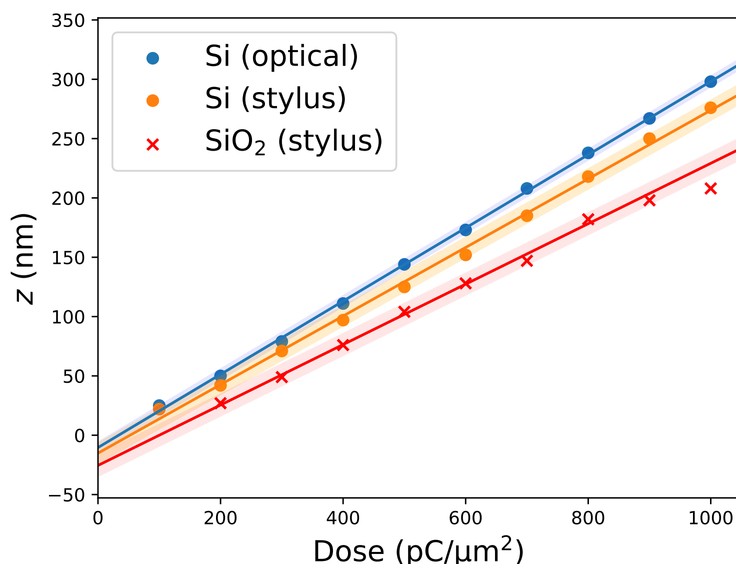

Figure 12. Experimental results from profilometry plotted as function of the dose and linear fits done for each measurement set with 95 % confidence interval.

intercept y-axis at zero with zero dose as should be expected. However, this can be explained as a result of change in the etch rate during first moments of the etch. At the beginning of the etch, the etched material is crystalline but going forward the sputtered material starts to redeposit and build on top of the substrate. Borgardt et al. [15] reported 1.3 times higher etching rate for redeposited Si compared to Si and similarly [28] reported 1.15 times higher etch rate for redeposited SiO_2 compared to crystalline SiO_2. With SiO_2 it takes longer to reach condition of pure redeposited material compared to Si, since the sputtering yield of crystalline SiO_2 is smaller than sputtering yield of Si, and therefore fit done for SiO_2 etch tests intercepts the y-axis further from zero. However, this error related to material composition change is systematic and can be observed in the beginning of each etch and therefore has no effect on the slope of the fit, which defines the etch rates.

3.2 Effect of gallium ion dose and implantation parameters

After the etch rates were determined, we wanted to find the optimal dose and implantation parameters beam blur and pitch with respect to the superconductive properties. High enough dose is needed to reach sufficient Ga concentration in silicon. However, higher doses take longer time to implant, thus it is beneficial to find needed minimal dose. Therefore, implantation was performed with doses 20 pC/µm^2, 50 pC/µm^2, 100 pC/µm^2, 200 pC/µm^2 and 500 pC/µm^2 while keeping the beam blur and pitch same as in etch rate tests in Sec. 3.1. However, to allow effortless electrical measurements, silicon substrates were coated with thin insulating thermal oxide SiO_2 and Al-metal contact pads were sputtered.

These sample chips were fabricated from basic 675 µm thick crystalline high-resistivity 150 mm diameter silicon wafers by first growing 30 nm thick thermal oxide on top and then sputtering the 300 nm thick Al-layer. After which a photolithography step was performed where contact pads for the measurements (Fig. 19 a)) were patterned. First, positive photoresist was applied and then exposed to ultraviolet (UV) light through a mask. After exposure the resist was developed, which means for positive resist that resist areas exposed to light were removed. Finally, area without the resist was etched away by plasma etching. Aluminium was overetched for 5 nm so that it was certain that there was no possibility for shorts caused by residue Al. This overetching also led to 5 nm thinner SiO_2 layer on the areas where Al was etched. After these steps wafers were then diced into smaller chips approximately 1 x 1 cm^2 with structures allowing multiple experiments on one chip.

Then the ion implantation with FIB was performed on these chips with the above mentioned doses. Implantation area was chosen so that it covered four Al-pads allowing accurate four-point measurements and contact between Al and created SiGa was obtained by depositing approximately 300 nm thick 5µm by 5µm Pt pads across the junction as shown in Fig. 13. The final layer structure of the samples is

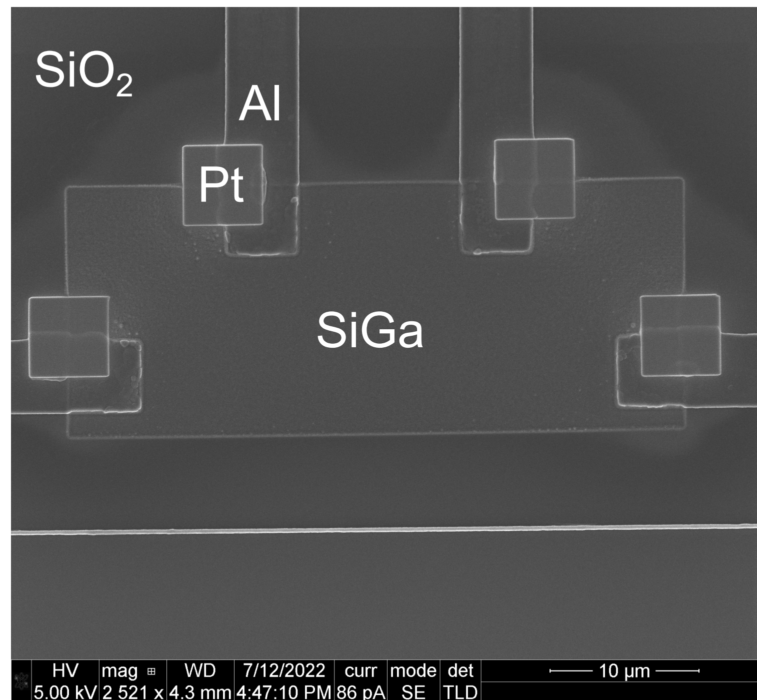

Figure 13. SEM image of sample fabricated with Ga dose 500 pC/µm^2, blur 200 nm and pitch 100 nm.

also shown in cross-section scheme in Fig. 14.

SEM image of the fabricated sample (Fig. 13) shows spreading of deposited Pt contacts observed in all the samples. Pt spreading can be seen as circular rings around the contacts. This kind of unwanted spreading is partly caused by deposition of residues on the sample through electron beam implantation when the SEM images are taken after the IBID. Implantation of residues can be mitigated by waiting longer, thus giving vacuum pumps more time to remove impurities from the tool chamber after IBID and before turning electron beam on. However, Pt contacts are spaced far enough from each other, so that there is no risk of creating electrical shorts through Pt between them.

Samples were then prepared for electrical measurements by cleaving them in smaller sizes and wire bonding the Al contact pads to the Heliox AC-V cryostat sample holder. Then the cryostat was cooled down and we measured the resistance

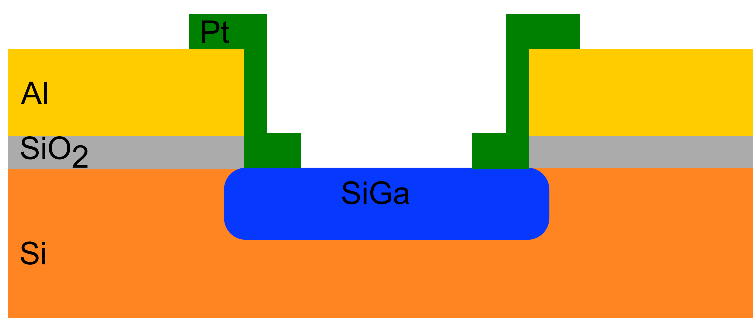

Figure 14. Schematic cross section of the final sample layer structure after Ga implantation and deposition of Pt contacts.

of each sample from room temperature down to 0.3 K and noticed that only samples implanted with doses 200 pC/µm^2 and 500 pC/µm^2 were conducting while other samples still after implantation had high resistance. Combined with the information coming from etch rate characterization in Sec. 3.1, we concluded that a dose of 100 pC/µm^2 is still not sufficient to reach metallic SiGa concentration, and at the same time the insulating behaviour is seen for 20 pC/µm^2 and 50 pC/µm^2 tests. Observing that SiO_2 implanted with Ga is not conductive was a great simplification for the study of the origin of the superconductivity in the samples.

In addition to the effect of the dose, we observed the effect of pitch and blur to the sample surface with SEM imaging. During the fabrication phase we varied pitch from 17.5 nm to 250 nm and blur between 100-500 nm. For comparison, implantation results of two samples implanted with same dose 500 pC/µm^2 and blur 500 nm but different pitches of 17.5 nm and 250 nm are shown in Fig. 15 a)-f). Implantation done with higher pitch shows clear rasterization pattern as a result of the ion beam scanning with large step size while the sample implanted with much smaller pitch does not show any rasterization even on the high magnification images. In comparison, quality of the sample implanted with the same dose but pitch 100 nm and blur 200 nm shown in Fig. 13 shows much less rasterization than the sample with pitch 250 nm. On the other hand sample with blur 200 nm is much smoother

than the one shown in Fig. 15 d) with 2.5 times larger blur and pitch. Comparing these images we can also notice that blur increases smoothing of the pattern edges which might have an effect on the properties of higher aspect ratio patterns. These results clearly advocate that small pitch and large blur are desired.

In addition to SEM imaging, we performed four-point measurements of large 40 µm x 20 µm SiGa area at the top of the sample with pitch 17.5 nm, shown in Fig. 15 a), the results of which are shown in Fig. 16. The measured four-point resistance is close in value to the sheet resistance due to aspect ratio 2 of the measured area. From these measurement results we can see that superconducting transition was reached near 6.3 K and the sample showed non-ohmic behaviour. We can also see that below 5.4 K the critical current I_c reached values greater than 80 µA. Critical current I_c for a given temperature is current passing through the studied material above which power dissipation starts to occur.

3.3 Optical measurements

Dielectric properties of SiGa were determined with ellipsometry. Before the measurement a large 500 x 470 μm^2 SiGa area was prepared via FIB implantation process on a basic 675 µm thick high-resistivity crystalline silicon substrate with approximately 25 nm thick SiO_2 layer on top. Large area is needed to perform NIR measurements due to needed spot size of the light. NIR measurements were used to determine properties of SiGa through model fitting. Due to limitations of the Helios 600, the large rectangle shaped area was implanted in three batches by slightly (approximately 5 nm) overlapping three separately implanted smaller rectangles. Implantation proces was performed with 30 kV acceleration voltage while the implanted dose was 300 pC/μm^2. Pitch and blur were kept same as previously. However, FIB current was increased to 21 nA to quicken the large area implantation process that would have taken an extended amount of time with sub-nA current.

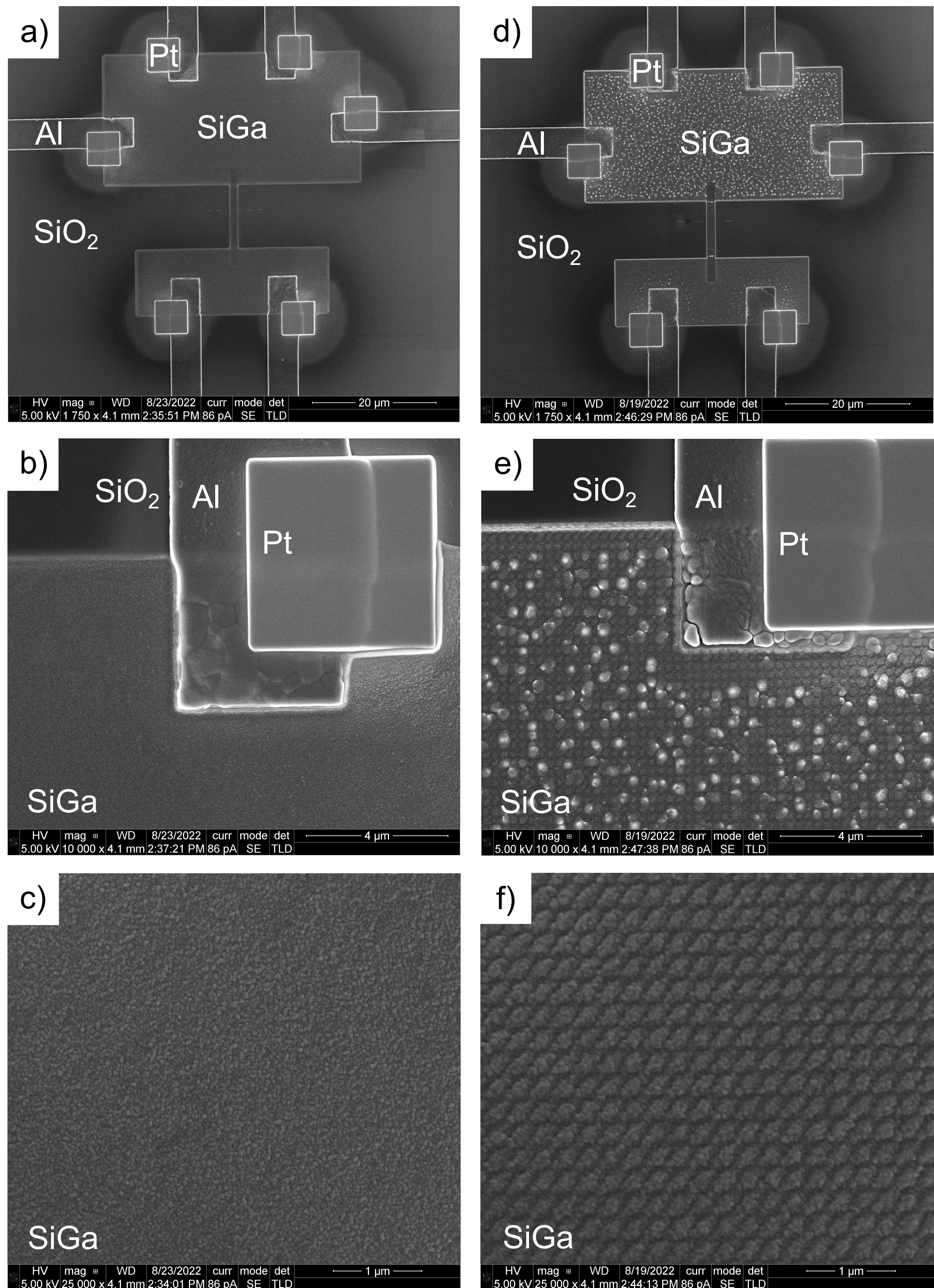

Figure 15. SEM images for comparison of Ga implantation with same dose 500 pC/μm^2 and blur 500 nm but with different pitches of a)-c) 17.5 nm and d)-f) 250 nm.

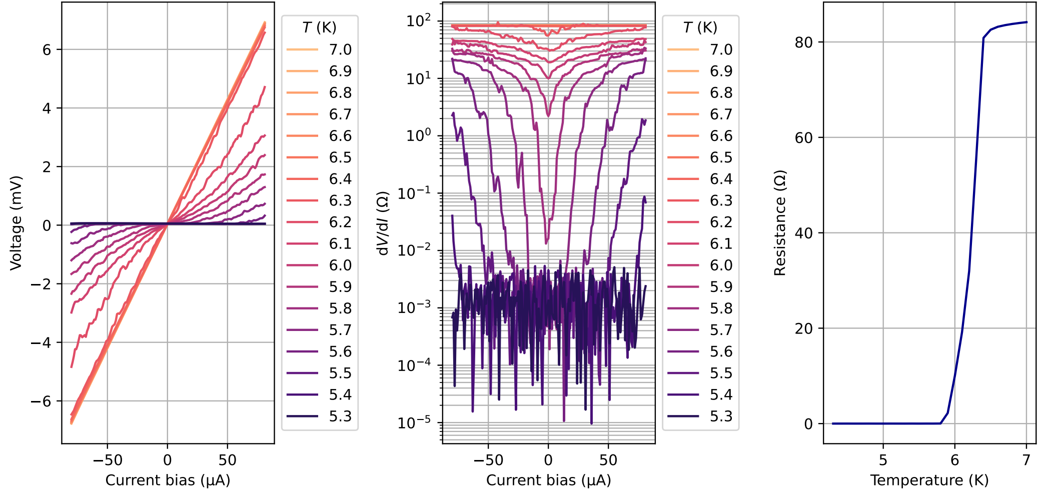

Figure 16. VI, RI and RT characteristics of large 40 µm x 20 µm SiGa area implanted with dose 500 pC/µm^2, pitch 17.5 nm and blur 500 nm.

After the implantation NIR measurements were performed with three different incident angle θ values 60°, 65° and 70°, varying wavelength between 750-2000 nm. Then, the gathered experimental data underwent data-analysis including fitting of the Drude free-electron model for the real and imaginary parts of ρ_R, shown in Fig. 17 and 18, which then produced parameters E_p and E_γ presented in Table II. Model fitting determined that SiGa thickness d was between 20-30 nm consistent with expectations from the used acceleration voltage. These measurements and data fits related to the ellipsometry were performed by a co-worker of the author.

From the above determined parameters it was possible to calculate the resistivity ρ and the electron concentration n of SiGa with equations (10) and (11). In calculations, we assumed that effective mass is equal to the mass of the electron for simplicity. Values for ρ and n were determined from the fit done for data measured with 60° incident angle were used in the following comparison, since that fit had the smallest chi-square (χ^2) value describing the fidelity between observed and modeled values. Thereby, for SiGa values $\rho \approx 7 \cdot 10^{-7}$ Ωm and $n \approx 4.5 \cdot 10^{22}$ 1/cm^3 were obtained. Above determined ρ and n for SiGa were then compared to values of liquid

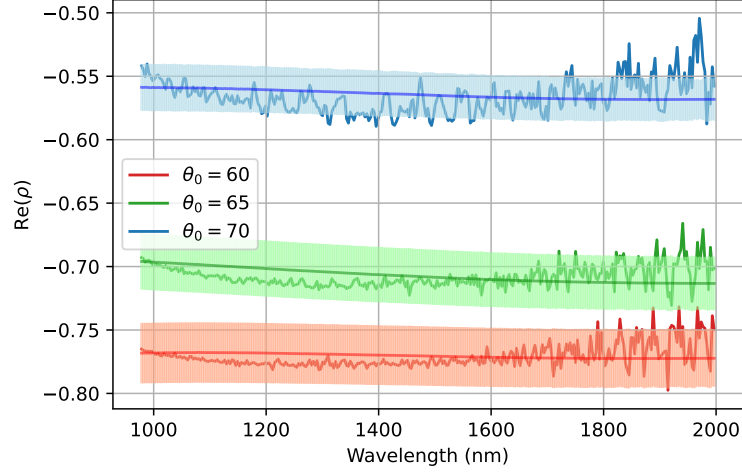

Figure 17. Measured real part of ρ_R as a function of wavelength and the Drude free-electron model fit for each angle of incidence with 3 % fitting tolerance band.

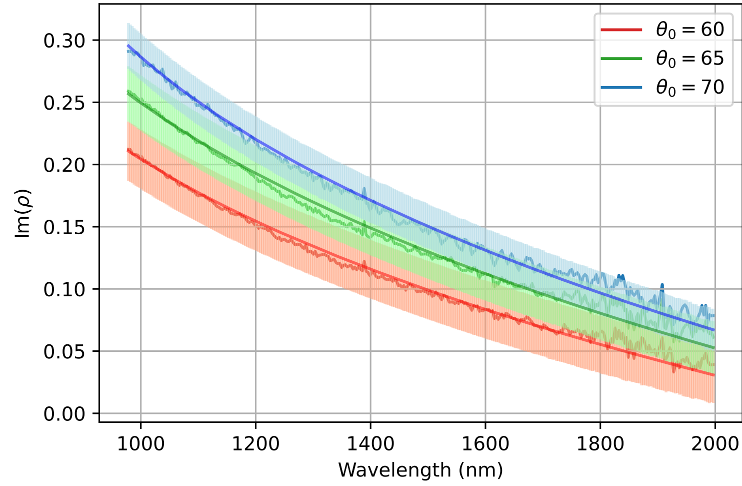

Figure 18. Measured imaginary part of ρ_R as a function of wavelength and the Drude free-electron model fit for each angle of incidence with 3 % fitting tolerance band.

Table II. Parameters found through fitting experimental ellipsometry data, and χ^2 value and relative estimate uncertainty of each fit parameter.

θ [°]	χ^2	E_p [eV]	ΔE_p	E_γ [eV]	ΔE_γ	d [nm]	Δd
60.0	72.8	7.909	0.47 %	0.594	1.26 %	27.04	0.53 %
65.0	103	8.249	0.39 %	0.609	1.45 %	24.02	0.56 %
70.0	261	7.369	0.39 %	0.599	1.70 %	20.54	0.56 %

Ga, which is a good example of a free-electron metal. We noticed that resistivity of SiGa was approximately 2.7 times the resistivity of liquid Ga ($\rho = 2.6 \cdot 10^{-7}$ Ωm) at its melting point 303 K and similarly electron concentration of SiGa was approximately 30 % of liquid gallium's electron concentration $15.7 \cdot 10^{22}$ 1/cm^3 calculated by multiplying the atomic density $5.22 \cdot 10^{22}$ atoms/cm^3 of liquid Ga at 350 K by three, which is the number of conduction electrons on the outer shell of Ga [29–31]. These results show that the resistivity of normal state SiGa compares reasonably with a diluted liquid gallium phase.

3.4 Nanowires and implant modulation

The superconductive properties of sheet SiGa were already shown in previous section, however we wanted to also demonstrate FIB capabilities on fabrication of superconductive SiGa nanowires. Additionally, the possibility of fabrication of superconductor-normal-superconductor (SNS) -like junctions allowing modulation of the p-type carriers in a implant discontinuity along the nanowires was studied. Boron doped p-type 725 µm thick crystalline silicon wafer with 50 Ωcm resistivity was now used instead of high-resistivity silicon. Similar fabrication process where 25 nm thermal oxide and 300 nm Al plating was used. However, after the sputtering of the Al plating, 45 nm thick hydrogen silsesquioxane (HSQ) lines of two different widths, 30 nm and 60 nm, were patterned with electron beam lithography (EBL) process between the Al pads as shown in Fig. 19 b) leading to sample layer structure shown in Fig. 20 a). We chose to use HSQ resist since it mainly consists of same materials and has similar structures as SiO_2 and was therefore expected to have similar etch rate. HSQ is also negative resist which means that the exposed area stays on the sample surface after EBL process and wash, and therefore only small areas needed to be exposed with electrons. Finally, wafers were diced into smaller chips and we performed the FIB Ga implantation.

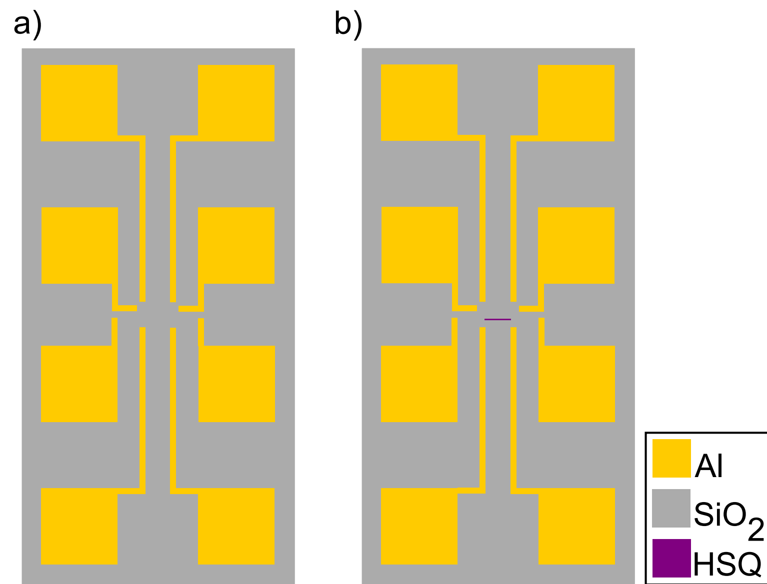

Figure 19. Schematic of a) Al metalization layout and b) schematic of Al metalization layout showing HSQ line placement.

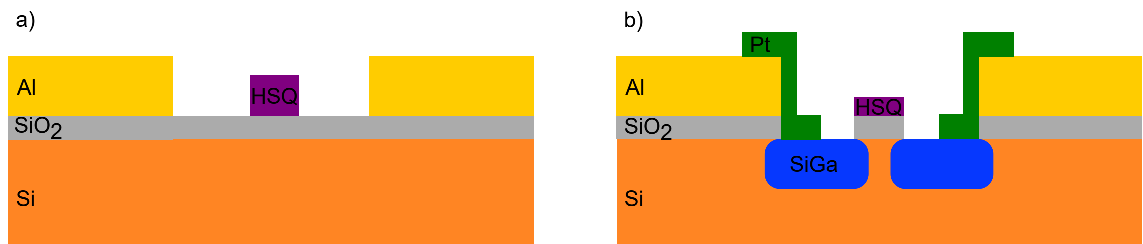

Figure 20. Schematic of a) sample before Ga implantation and b) expected sample after Ga implantation and Pt deposition. However, due to etching properties of high aspect ratio features, expected sample structure was not met.

We used 500 nm blur and 17.5 nm pitch to create smooth surfaces while acceleration voltage and beam current were kept at usual 30 kV and 0.46 nA. First, implantation was done on two chips both with two samples. One of these samples had 30 nm and the other 60 nm wide HSQ line allowing the study of the effect of the HSQ line width. Dose 500 pC/µm^2 was used for one chip and dose 200 pC/µm^2 for the other. The implantation of one sample was done in three steps so that first the larger areas with dimensions of 40 µm x 20 µm and 30 µm x 10 µm were implanted across the Al pads and then these areas were connected with implanted 500 nm wide and approximately 10 µm long nanowire by slightly overlapping with large areas as shown in Fig. 21 on configuration enabling four-point measurements of the largest SiGa area and the nanowire. The effect on the surface due to overlapping the nanowire is shown in Fig. 22 where areas with different doses are clearly marked and the height differences, which possibly have an effect on the electrical properties, can be seen.

The expected layer structure after ion implantation and Pt contact deposition is shown in Fig. 20 b). However, from SEM images of the nanowire (Fig. 23) and close-up of the HSQ line (Fig. 24) implanted with dose 200 pC/µm^2, which is the minimum dose needed according to Sec. 3.2, it seems like HSQ had no masking effect on the etching of the oxide layer. To confirm this, particular sample's surface structure was further studied with atomic force microscopy (AFM). Step height measurements of the unetched and etched HSQ lines (Fig. 25) show that the HSQ mask is etched away much quicker on a pace approximately 8 times the anticipated planar SiO_2 etch rate leaving only slight widened shade of the HSQ line. This kind of behavior can be expected with high aspect ratio structures as these HSQ lines, since the sputtering yield is significantly higher for the vertical sidewalls of the HSQ lines, compared to planar SiO_2 etch rate values. As a consequence, thin HSQ masks cannot withstand even the minimal dose required for superconducting SiGa implantation. However,

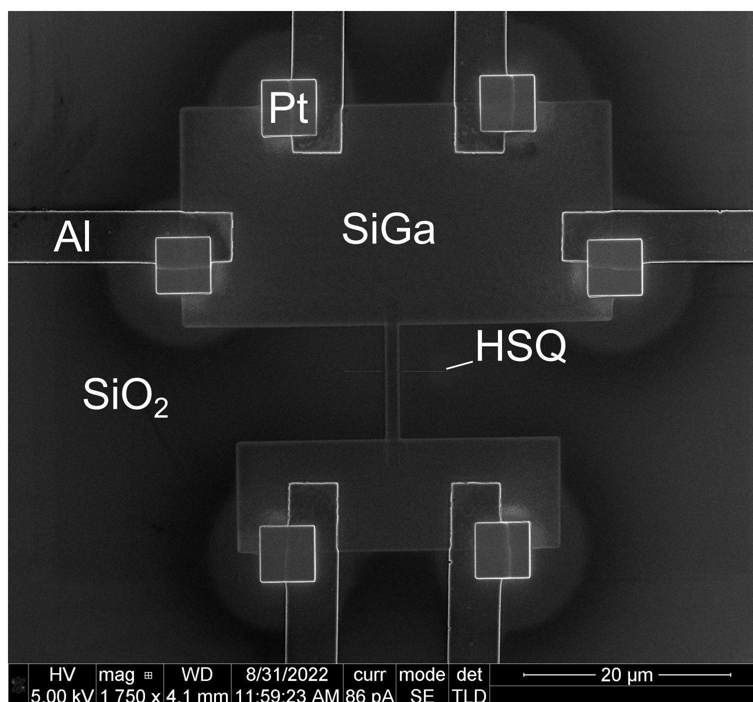

Figure 21. SEM image of sample fabricated with dose 350 pC/μm^2.

these results did not give high hopes for acquiring the desired physical and electrical properties with this technique since even with the smallest used dose the resist had barely an effect on the nanowire structure.

Nevertheless, chips having the above described four samples were cleaved and wire bonded to the sample holder as shown in Fig. 26. Then samples were cooled down in the cryostat similarly as in Sec. 3.2 and electrical measurements were performed. First, four-point resistance of each implanted large area was measured as a function of temperature (Fig. 27) similarly as in Sec. 3.2 and clearly only the samples implanted with the dose 500 pC/μm^2 showed T_c located above 6 K while samples with the smaller dose 200 pC/μm^2 were almost at the MIT but still metallic and barely conducting.

Since samples implanted with the dose 500 pC/μm^2 showed superconductivity on large area we took a closer look at the 500 nm x 10 μm nanowires implanted with same dose and performed more measurements on them shown in Fig. 28 a) and b).

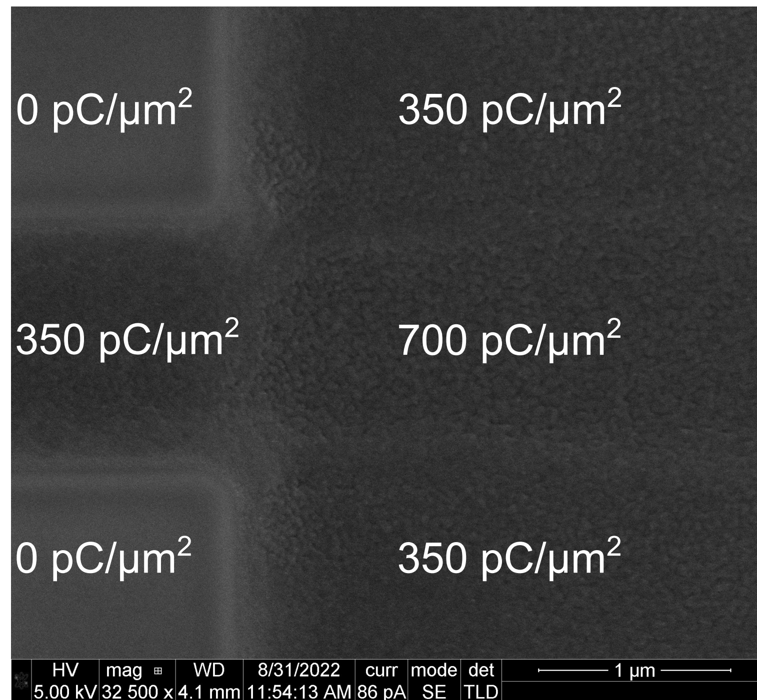

Figure 22. SEM image of the overlapping connection of horizontal nanowire implanted with dose 350 pC/µm^2. Total doses for the areas are marked in the image where the overlapping area has dose 700 pC/µm^2.

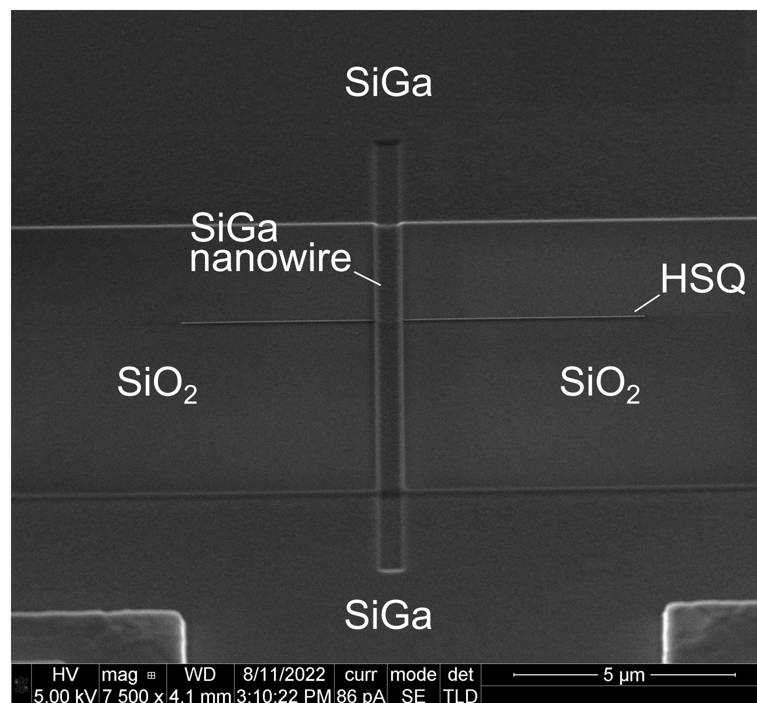

Figure 23. SEM image of nanowire implanted with dose 200 pC/µm^2.

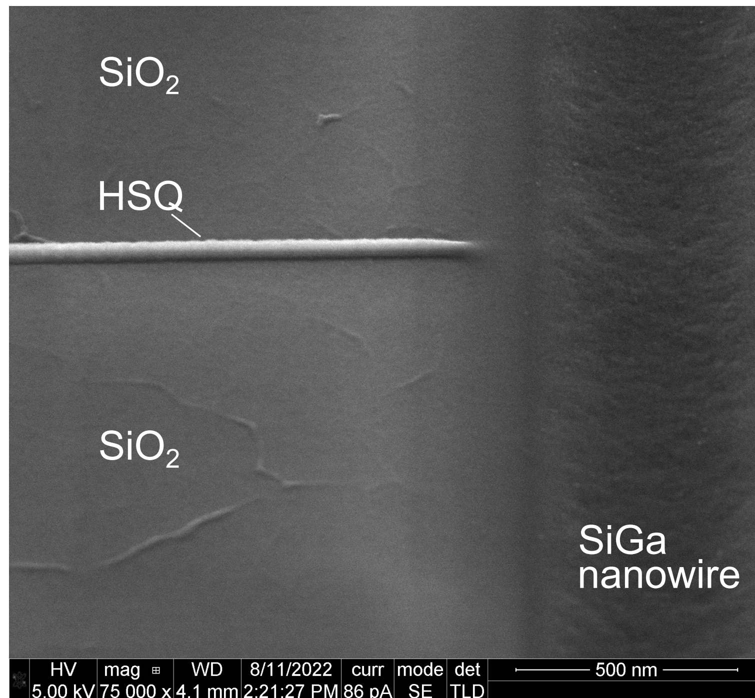

Figure 24. SEM image of etched HSQ line on a nanowire implanted with dose 200 pC/µm^2.

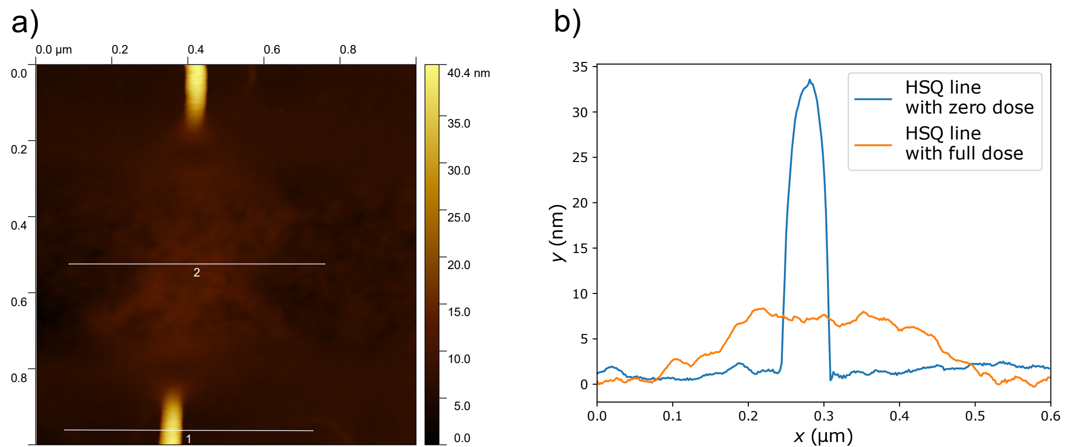

Figure 25. a) AFM image of HSQ line crossing horizontal (left to right) nanowire implanted with dose 200 pC/µm^2. White lines correspond to extracted line profiles of HSQ with (1) zero dose and (2) full dose. b) Extracted AFM line profiles with zero and full dose. With zero dose the HSQ line profile was clear high aspect ratio structure but with full dose all the HSQ was etched and only widened imprint from the shading of the HSQ line was observed.

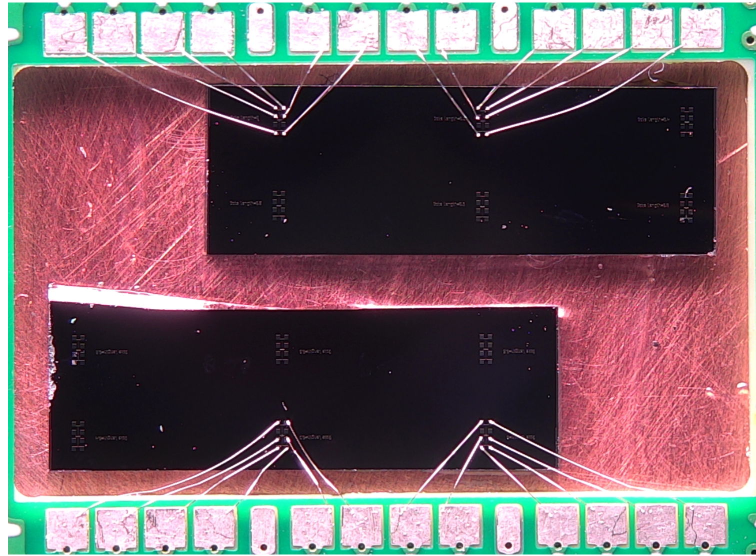

Figure 26. Samples cleaved and wire bonded, ready to be set in the cryostat for electrical measurements. Six contacts were made to each sample to allow four-point measurements of largest SiGa areas and nanowires.

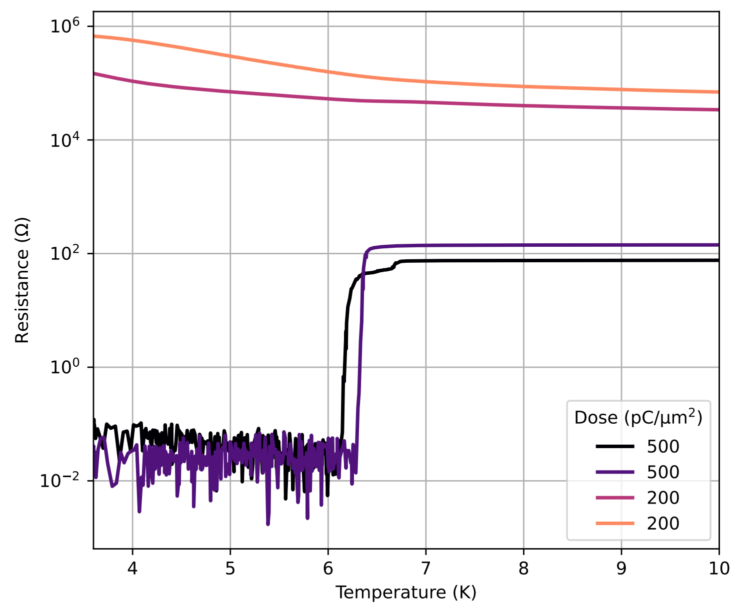

Figure 27. Measured four-point resistances of 40 µm x 20 µm areas of independent samples, two fabricated with dose 200 pC/µm^2 and the other two with dose 500 pC/µm^2, as a function of temperature.

Both nanowires behaved similarly and the HSQ line width had no effect on the properties as can be seen aforementioned Fig. 28 a) and b). Nanowires were not superconductive and measurement setup limit resistance 10^{11} Ω was reached at 0.3 K but they showed non-ohmic behaviour still at near 10 K temperatures. The middle plots with differential conductivity $\mathrm{d}I/\mathrm{d}V$ as a function of voltage bias shows that at low temperatures 40 mV voltage bias was needed to overcome the energy gap and increase the conductivity while from the rightmost plot with zero bias differential resistance $\mathrm{d}V/\mathrm{d}I$ as a function of temperature the saturation of resistance at low temperatures can be seen. Since the nanowire has clearly high amount of series resistance but still shows non-ohmic behaviour, it has at least some conducting parts.

Since, dose 200 pC/µm^2 seemed too low to reach superconducting state, a new set of six samples with doses of 350 pC/µm^2 and 500 pC/µm^2 were fabricated to further study the effect of the HSQ line and effect of the nanowire width. Again, samples were fabricated on two separate chips, one implanted with dose 350 pC/µm^2 having four samples total and the other with 500 pC/µm^2 having two samples. Now, the width of the nanowire was changed between 500 nm and 1000 nm and control nanowire samples without HSQ were implanted corresponding to each sample with HSQ. Control wire samples with nanowires implanted between two 17.5 µm x 17.5 µm SiGa squares (Fig. 29) were also configured so that four-point measurements were possible.

We performed similar measurements for these samples as for the first nanowire samples. Both 500 nm nanowire and control nanowire without HSQ implanted with dose 350 pC/µm^2 showed comparable results to above characterized 500 nm nanowires implanted with dose 500 pC/µm^2 as can be seen from Fig. 30 a) and b). However, all samples with wider 1000 nm nanowires (Fig. 31 and 32) were superconductive even with the lower dose 350 pC/µm^2. Critical temperatures near 6.3 K and

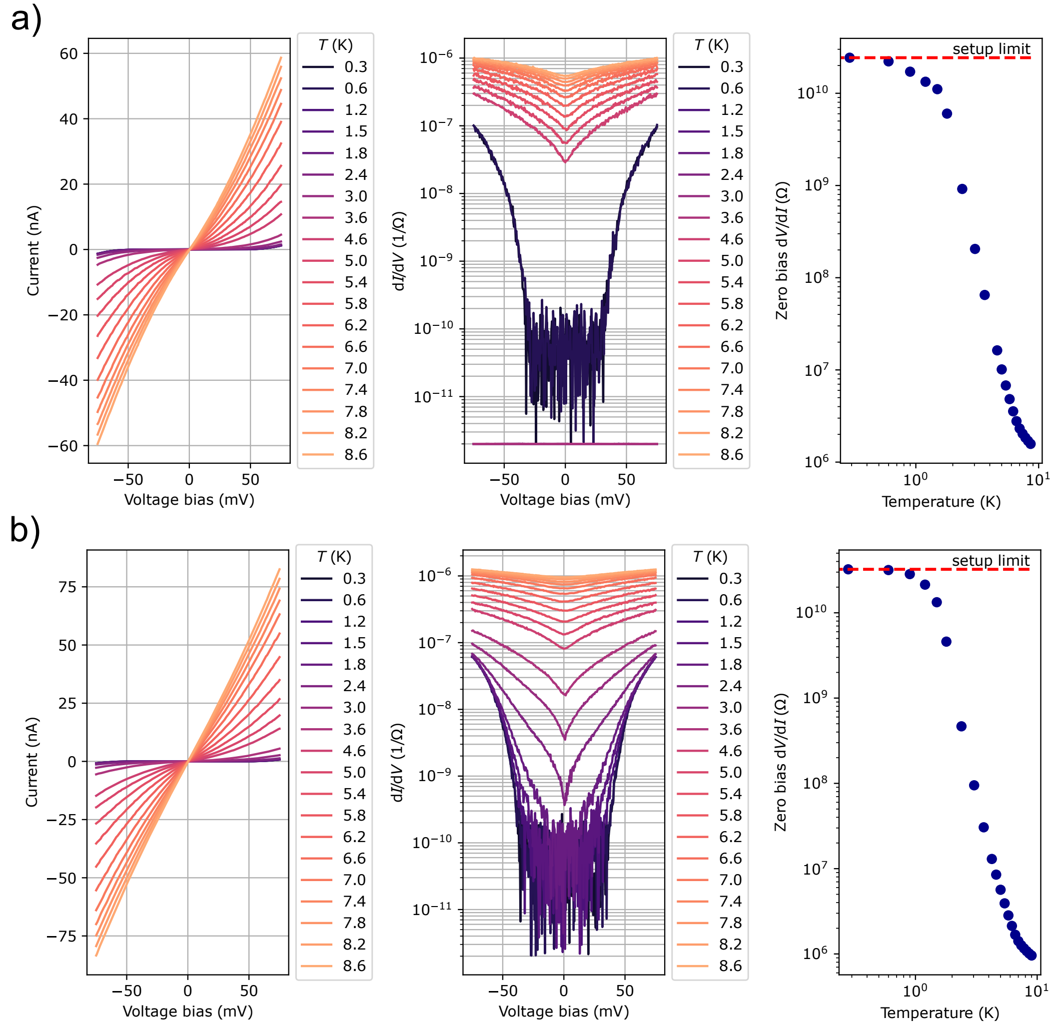

Figure 28. IV, IR and RT characteristics of 500 nm nanowires with a) 30 nm and b) 60 nm HSQ lines, implanted with dose 500 pC/µm^2.

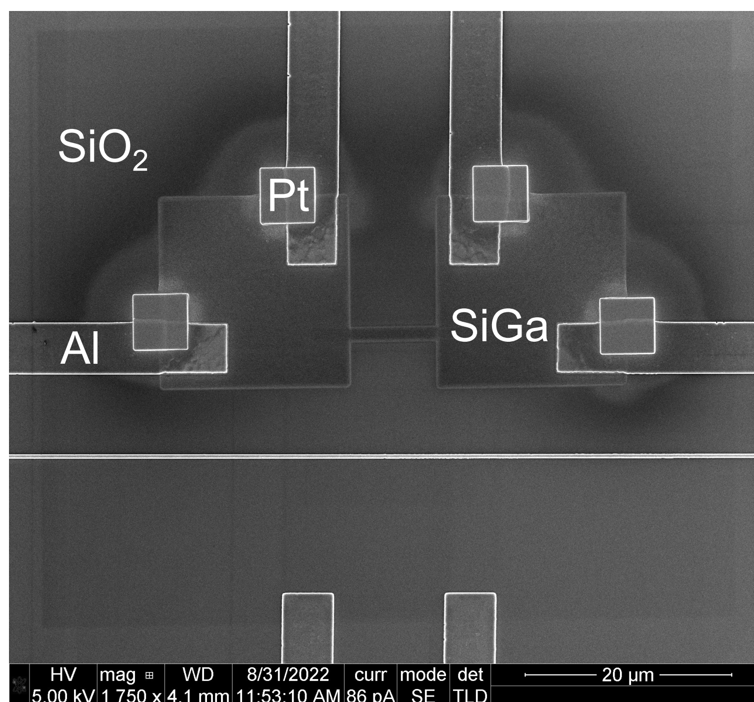

Figure 29. SEM image of the control sample layout implanted with dose 350 pC/µm^2.

critical currents up to 70 µA at 4.4 K were observed with the higher dose while with the lower dose critical currents reached only approximately 30 µA. These critical currents are fairly high when compared to previously measured I_c of much larger 40 µm x 20 µm implanted with same 500 pC/µm^2 dose. Even though we could estimate the cross sectional area of SiGa based on the used implantation voltage, the critical current density J_c was not calculated for any of the samples since the part of SiGa depth distribution, which corresponds to the superconductivity in unknown. Simultaneously we confirmed that HSQ lines had no appreciable effect on the electrical properties by comparing the results of similar nanowires with HSQ line and control nanowires without HSQ line. On the other hand, we also discovered that surprisingly the nanowire width had an effect on the superconductive properties.

Due to observation above, we measured the profile of one of the nanowires implanted with high 500 nm blur shown in Fig. 33. Instead of having vertically-etched

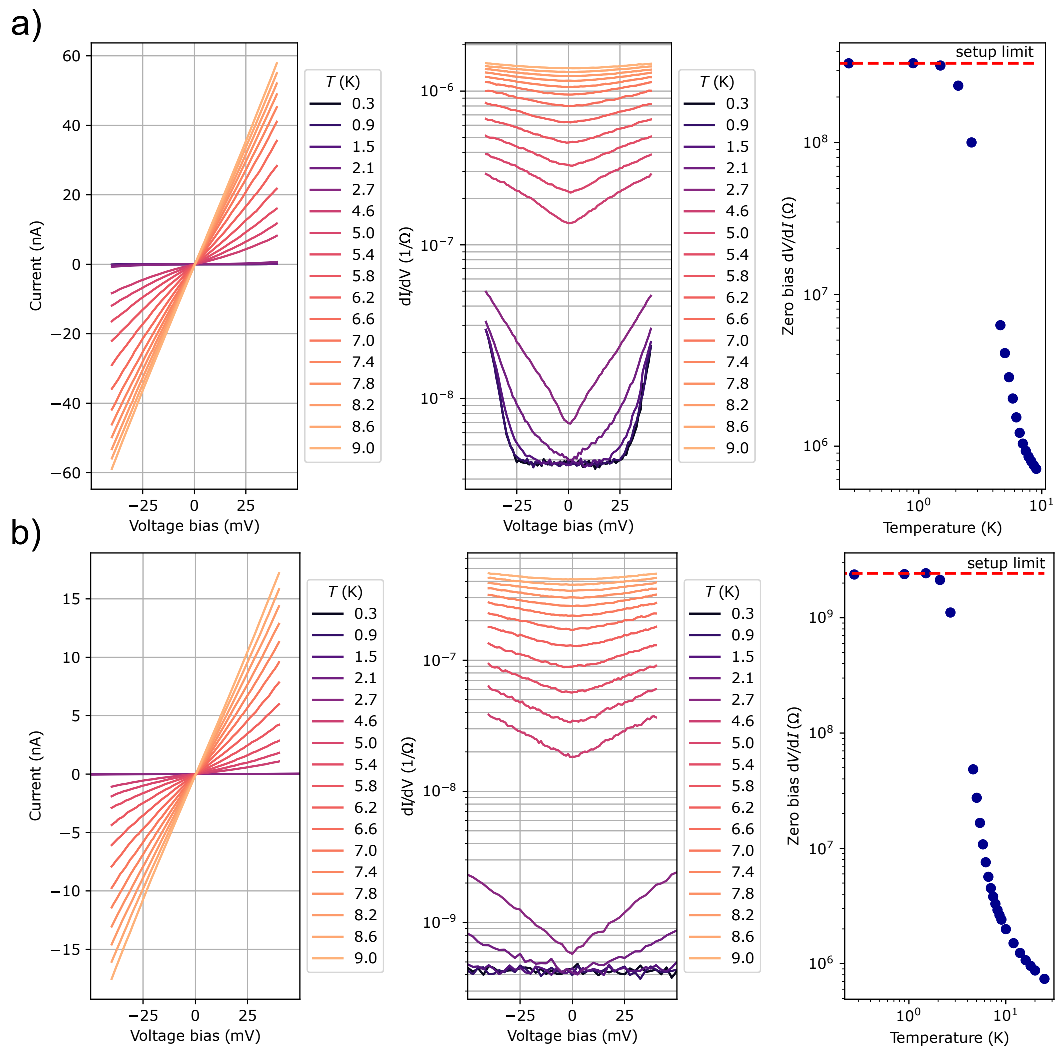

Figure 30. IV, IR and RT characteristics of sample with 500 nm wide a) nanowire and b) nanowire control sample both implanted with dose 350 pC/µm^2.

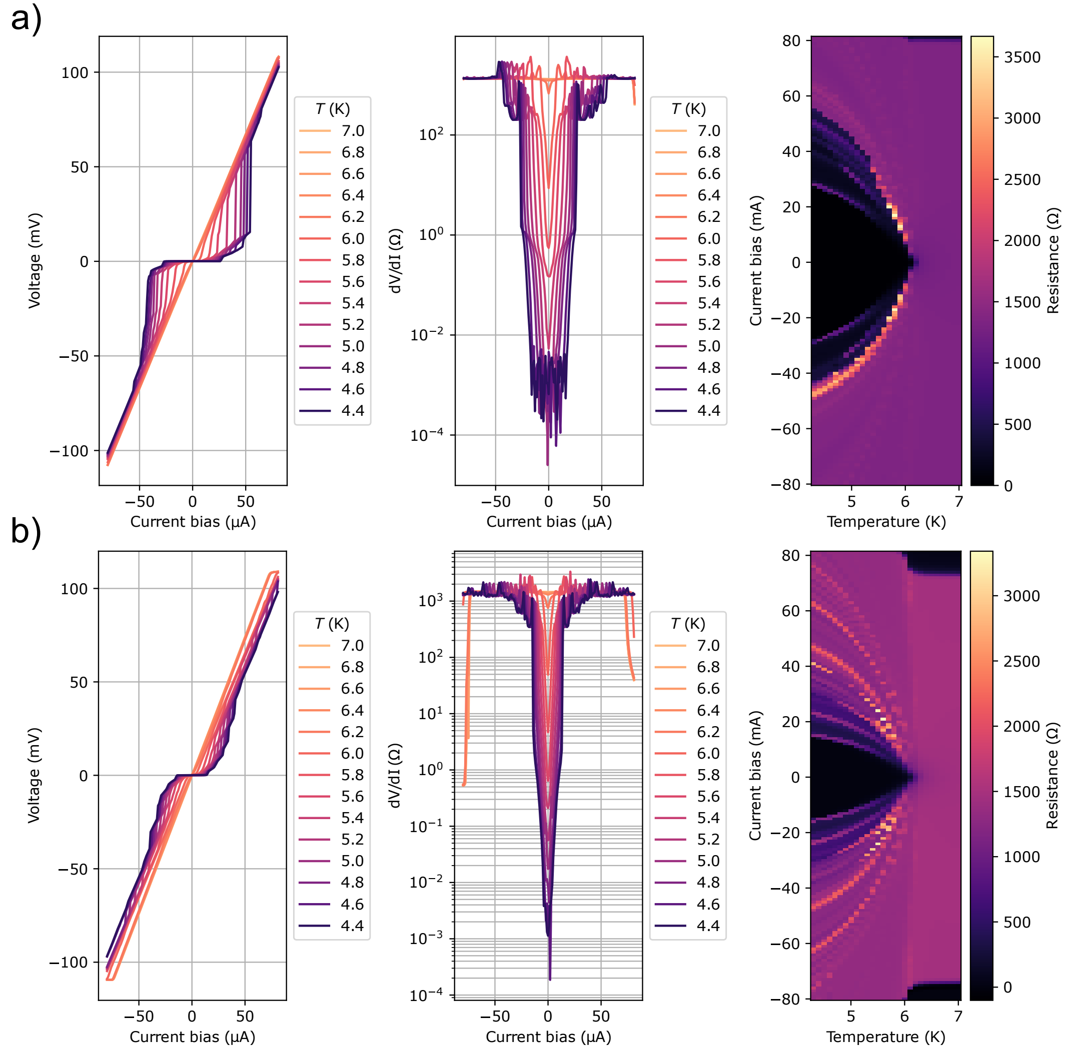

Figure 31. IV, IR and RT characteristics of sample with 1000 nm wide a) nanowire and b) nanowire control sample both implanted with dose 350 pC/µm^2. Areas above 6 K with zero resistance and 80 µA current biases in RT characteristics of the nanowire control sample are a result of saturation of voltage preamplifier range.

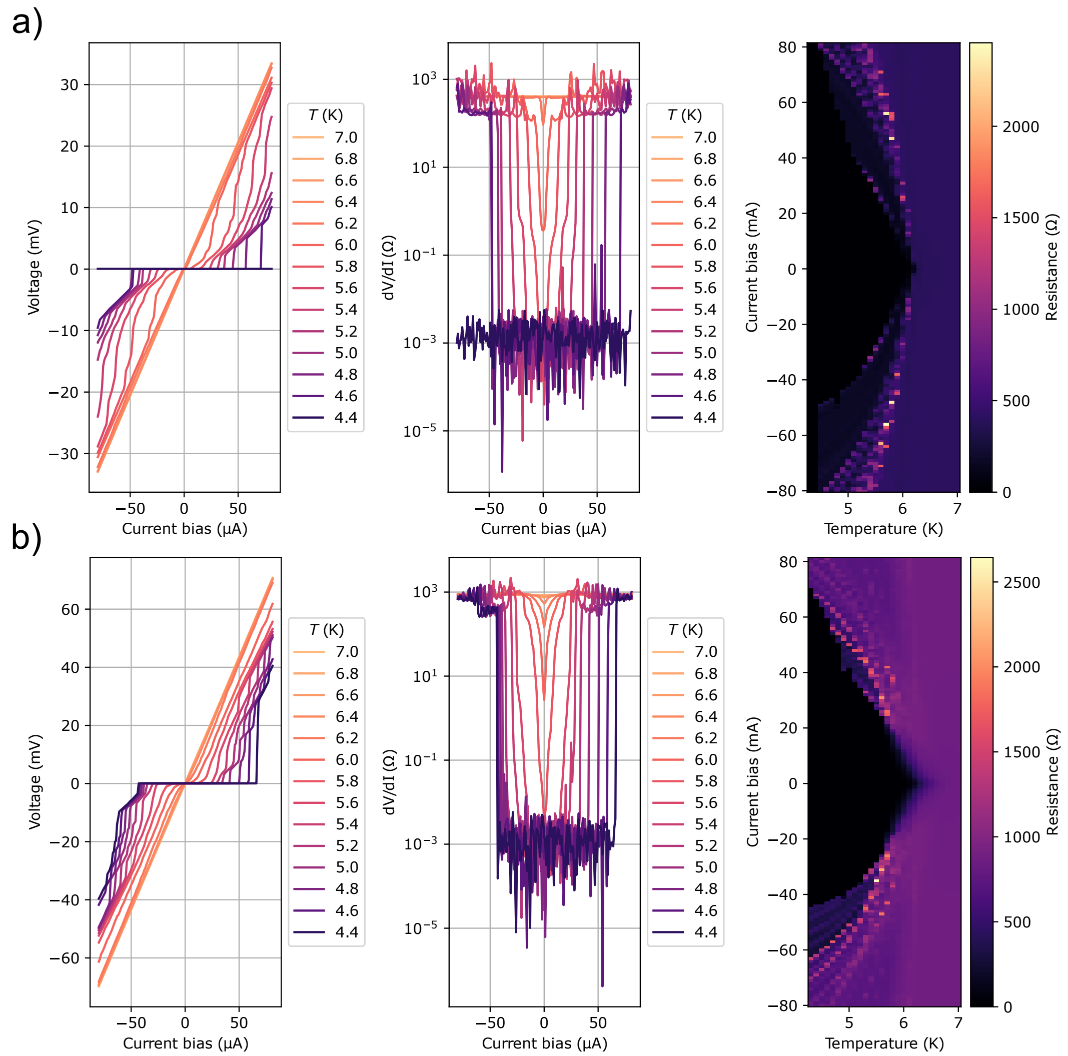

Figure 32. IV, IR and RT characteristics of sample with 1000 nm wide a) nanowire and b) nanowire control sample both implanted with dose 500 pC/µm^2.

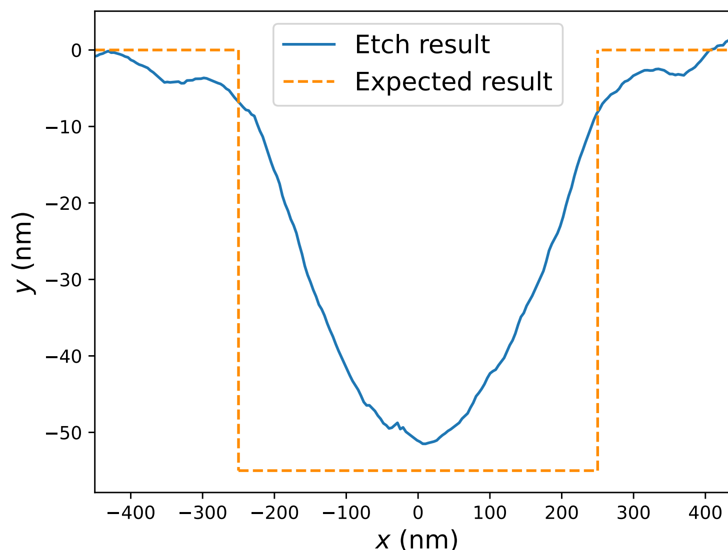

Figure 33. AFM step height measurement and expected result of the etch of the nanowire implanted with dose 200 pC/µm^2 and blur 500nm.

edges, nanowires implanted with the high blur were V-shaped, which was the result of blur spreading the dose to wider area and therefore decreasing the dose per area. This kind of edge smoothing was mentioned already in Sec. 3.2. When the V-shape starts to form, etching is no more performed on a horizontal plane but instead on an inclined plane. This increases redeposition, which can be one reason for non-superconductive nanowires, since redeposited silicon has lower Ga concentration as can be seen from Fig 2. Also, expected depth of 55 nm with the dose 200 pC/µm^2 through 25 nm SiO_2 layer and silicon calculated with the ion beam etch rate values determined in Sec. 3.1 was not fully reached. Instead, the maximum etching depth observed was approximately 50 nm.

4 Conclusion

In this thesis, fabrication and characteristics of superconducting silicon-gallium alloy were studied. Essential background to superconductivity in covalent-bound materials was given and experimental methods both for fabrication and characterization

were discussed.

At first, the etch rate of the focused Ga-ion beam was determined and effect of implant dose confirmed. Simultaneously implantation parameters were improved based on the observations. Finally, superconductive nanowires were fabricated and implant modulation with HSQ mask was investigated. Nanowires were characterized with electrical measurements and their surface topography was studied.

Superconductive transition was observed approximately at 6.3 K with both large areas and nanowires when sufficient doses above 200 pC/μm^2 were used. Unfortunately, implant modulation with high aspect ratio HSQ lines was not successful due to increased etch rate of vertical sidewalls of the HSQ lines. However, the effect of the implanted nanowire width to superconductive properties was discovered and discussed.

In the future, different methods should be tested to enable implant modulation and fabrication of refined nanowires to allow implementation of more complicated structures. Additionally, critical current scaling with wire cross section will be investigated to provide assessment of critical current density and effect of magnetic field will be studied. Also, a feasibility study on different types of substrates, such as amorphous silicon, has been planned.

References

[1] E. Bustarret *et al.*, Nature **444**, 465 (2006).

[2] R. Skrotzki *et al.*, Applied Physics Letters **97**, 10 (2010).

[3] C. P. Poole, H. A. Farach, R. J. Creswick, and R. Prozorov, *Superconductivity* (Elsevier Science & Technology , 2007).

[4] J. Bardeen, L. N. Cooper, and J. R. Schrieffer, Phys. Rev. **108**, 1175 (1957).

[5] M. Tinkham, *Introduction to superconductivity*, 2nd ed. (Dover Publications , 2004).

[6] M. L. Cohen, Physical Review **134**, (1964).

[7] G. Grosso, *Solid state physics* (Academic Press , 2000).

[8] E. A. Ekimov *et al.*, Nature **428**, 542 (2004).

[9] B. Stritzker and H. Wühl, Zeitschrift für Physik B Condensed Matter **24**, 367 (1976).

[10] M. S. Osofsky *et al.*, Physical Review Letters **87**, 197004/1 (2001).

[11] A. Grockowiak *et al.*, Physical Review B - Condensed Matter and Materials Physics **88**, 1 (2013).

[12] H. Statz, Journal of Physics and Chemistry of Solids **24**, 699 (1963).

[13] V. Heera *et al.*, Applied Physics Letters **100**, (2012).

[14] V. Heera *et al.*, New Journal of Physics **15**, (2013).

[15] N. I. Borgardt, A. V. Rumyantsev, R. L. Volkov, and Y. A. Chaplygin, Materials Research Express **5**, 25905 (2018).

[16] R. Matsumoto *et al.*, ACS Applied Electronic Materials **2**, 677 (2020).

[17] D. Campanini, Z. Diao, and A. Rydh, Physical Review B **97**, 2 (2018).

[18] L. A. Giannuzzi and F. A. Stevie, *Introduction to Focused Ion Beams: Instrumentation, Theory, Techniques and Practice*, 1. aufl. ed. (Springer Science + Business Media , 2006).

[19] C. A. Volkert and A. M. Minor, MRS bulletin **32**, 389 (2007).

[20] M. Nastasi and J. W. Mayer, *Ion implantation and synthesis of materials* (Springer-Verlag , 2006).

[21] A. W. Czanderna, T. E. Madey, and C. J. Powell, *Beam effects, surface topography, and depth profiling in surface analysis*, 1st ed. 2002. ed. (Plenum Press New York, 1998).

[22] B. Griffiths, *Manufacturing surface technology surface integrity & functional performance* (Taylor & Francis , 2001).

[23] D. K. Schroder, *Semiconductor material and device characterization*, 3rd ed. ed. (Wiley , 2006).

[24] M. Sardela, *Practical materials characterization* (Springer New York , 2014).

[25] S. A. Maier, *Plasmonics: Fundamentals and Applications: Fundamentals and Applications*, 1. aufl. ed. (Springer Science + Business Media , 2007).

[26] I. Sakho, *Introduction to Quantum Mechanics 1: Thermal Radiation and Experimental Facts Regarding the Quantization of Matter* (John Wiley & Sons, Incorporated , 2019).

[27] *SEA User's Reference Manual*, Semilab Co. Ltd., 2020.

[28] A. V. Rumyantsev, N. I. Borgardt, R. L. Volkov, and Y. A. Chaplygin, Vacuum **202**, (2022).

[29] M. J. Assael *et al.*, Journal of Physical and Chemical Reference Data **41**, 33101 (2012).

[30] F. Greuter and P. Oelhafen, Zeitschrift für Physik B Condensed Matter **34**, 123 (1979).

[31] L. H. Xiong *et al.*, Acta Materialia **128**, 304 (2017).